PLOS BIOLOGY

RESEARCH ARTICLE

# SNX27–Retromer directly binds ESCPE-1 to transfer cargo proteins during endosomal recycling

**Boris Simonetti[1☯]*, Qian Guo[2☯], Manuel Giménez-Andrés[1☯], Kai-En Chen[2], Edmund R. R. Moody[3], Ashley J. Evans[1], Mintu Chandra[2], Chris M. Danson[1], Tom A. Williams[3], Brett M. Collins[2]*, Peter J. Cullen[1]***

**1** School of Biochemistry, Faculty of Life Sciences, University of Bristol, Bristol, United Kingdom, **2** Institute for Molecular Bioscience, The University of Queensland, St. Lucia, Queensland, Australia, **3** School of Biological Sciences, Faculty of Life Sciences, University of Bristol, Bristol, United Kingdom

☯ These authors contributed equally to this work.
* bsimonetti@hotmail.com (BS); b.collins@imb.uq.edu.au (BMC); pete.cullen@bristol.ac.uk (PJC)



OPEN ACCESS

**Citation:** Simonetti B, Guo Q, Giménez-Andrés M, Chen K-E, Moody ERR, Evans AJ, et al. (2022) SNX27–Retromer directly binds ESCPE-1 to transfer cargo proteins during endosomal recycling. PLoS Biol 20(4): e3001601. https://doi.org/10.1371/journal.pbio.3001601

**Academic Editor:** Maya Schuldiner, Weizmann Institute of Science, UNITED STATES

**Received:** September 22, 2021

**Accepted:** March 11, 2022

**Published:** April 13, 2022



**Data Availability Statement:** All relevant data are within the paper and its Supporting Information files.

**Funding:** Work in the Cullen laboratory is supported by the Wellcome Trust (104568/Z/14/Z and 220260/Z/20/Z), the Medical Research Council (MR/L007363/1 and MR/P018807/1), the Lister Institute of Preventive Medicine, and the award of a Royal Society Noreen Murray Research Professorship to P.J.C. (RSRP/R1/211004). B.M.C. is supported by a Senior Research Fellowship and

## Abstract

Coat complexes coordinate cargo recognition through cargo adaptors with biogenesis of transport carriers during integral membrane protein trafficking. Here, we combine biochemical, structural, and cellular analyses to establish the mechanistic basis through which SNX27–Retromer, a major endosomal cargo adaptor, couples to the membrane remodeling endosomal SNX-BAR sorting complex for promoting exit 1 (ESCPE-1). In showing that the SNX27 FERM (4.1/ezrin/radixin/moesin) domain directly binds acidic-Asp-Leu-Phe (aDLF) motifs in the SNX1/SNX2 subunits of ESCPE-1, we propose a handover model where SNX27–Retromer captured cargo proteins are transferred into ESCPE-1 transport carriers to promote endosome-to-plasma membrane recycling. By revealing that assembly of the SNX27:Retromer:ESCPE-1 coat evolved in a stepwise manner during early metazoan evolution, likely reflecting the increasing complexity of endosome-to-plasma membrane recycling from the ancestral opisthokont to modern animals, we provide further evidence of the functional diversification of yeast pentameric Retromer in the recycling of hundreds of integral membrane proteins in metazoans.

## Introduction

A central role of the endosomal–lysosomal network is to determine the sorting of integral proteins and their associated proteins and lipids, collectively termed "cargos," between 2 fates, either degradation within lysosomes or retrieval from this fate for the promotion of recycling to a variety of organelles that include the cell surface [1]. Efficient and selective endosomal–lysosomal cargo sorting is essential for the function of all eukaryotic cells with increasing evidence pointing to defects in endosomal retrieval and recycling being at the heart of a wide array of human diseases, most notably those associated with neurodegeneration [2]. Establishing the molecular mechanisms and functional significance of endosomal cargo retrieval and recycling is therefore fundamental to understand eukaryotic cell biology.

Project Grant from the National Health and Medical Research Council (APP1136021 and APP1156493). E.R.R.M. is supported by a Research Fellows Enhancement Award to T.A.W (RGF\EA\180199). T.A.W. is supported by a Royal Society University Fellowship (URF\R\201024). The funders had no role in study design, data collection and analysis, decision to publish, or preparation of the manuscript.

**Competing interests:** The authors have declared that no competing interests exist.

**Abbreviations:** aDLF, acidic-Asp-Leu-Phe; β-ME, β-mercaptoethanol; BAR, Bim/Amphiphysin/Rvs; BIC, Bayesian information criterion; ESCPE-1, endosomal SNX-BAR sorting complex for promoting exit 1; ITC, isothermal titration calorimetry; LIC, ligation-independent cloning; MGP, Mnemiopsis Genome Project Portal; NTA, nitrilotriacetic acid; PDZbm, PDZ-binding motif; RNAi, RNA interference; SEC, size-exclusion chromatography; SNX1, sorting nexin-1; SNX3, sorting nexin-3; SNX27, sorting nexin-27; WASH, Wiskott–Aldrich syndrome protein and SCAR homologue.

Two general concepts are considered to account for the mechanism of endosomal cargo retrieval and recycling. Sequence-independent sorting posits that sorting can proceed without the need for any sequence information within the intracellular cytoplasmic domains of integral membrane cargos [3]. On the other hand, sequence-dependent sorting is controlled by specific signals in the cytoplasmic domain of cargos. These signals are typically short linear peptide motifs that direct the sorting process through coupling to ancient and evolutionary conserved coat complexes [1,4,5]. In coupling sorting motif recognition with membrane remodeling, these coats coordinate the process of cargo retrieval with the formation of cargo-enriched transport carriers for onward recycling. In mammals, these coats include sorting nexin-3 (SNX3)-Retromer [6–10], SNX27–Retromer [11–14], SNX17–Retriever [15], the CCC (CCDC22/CCDC93/COMMD) [16,17], and endosomal SNX-BAR sorting complex for promoting exit 1 (ESCPE-1) complexes [18,19] and various accessory proteins including the actin polymerizing Wiskott–Aldrich syndrome protein and SCAR homologue (WASH) complex [20,21].

Sorting nexin-27 (SNX27) is an endosome-associated cargo adaptor composed of a central PX (phox homology) domain flanked by an amino-terminal PDZ (PSD95, disks large, and zona occludens) domain and a carboxyl-terminal FERM (4.1/ezrin/radixin/moesin) domain [22,23]. The PDZ domain recognizes a specific sorting motif, termed the PDZ-binding motif (PDZbm), present at the very carboxyl termini of over 400 cargo proteins including receptors, transporters, channels, enzymes, and adhesion molecules [11–13,23–31]. In recognizing these internalized cargos, SNX27 regulates their retrieval from lysosomal degradation and promotes their recycling back to the plasma membrane [11–13].

To facilitate the retrieval process, the SNX27 PDZ domain associates with Retromer, a stable heterotrimer of VPS26 (A and B isoforms expressed in humans [32]), VPS35 and VPS29, to form the SNX27–Retromer [12–14]. Retromer itself assembles to form dimeric arches that may cluster SNX27 captured cargos [9,10,33] and associates with the WASH complex to allow the localized Arp2/3-dependent polymerization of branched filamentous actin [34,35]. In a poorly understood process, these assemblies and actin dynamics are proposed to generate a retrieval subdomain on the endosomal membrane that is enriched in cargo destined for recycling [35–39]. It is from these subdomains that further membrane remodeling ensues to drive the biogenesis of cargo-enriched tubular profiles and tubulovesicular carriers that physically transport cargo back to the cell surface. Importantly, defects in SNX27–Retromer function are associated with the pathoetiology of human disease most notable neurological disorders and neurodegenerative disease [40].

A membrane tubulating Bin/Amphiphysin/Rvs (BAR) domain-containing protein associated with SNX27–Retromer tubular profiles is sorting nexin-1 (SNX1) [12]. SNX1, and its functional ortholog SNX2, is part of the ESCPE-1 complex [18,19,41], a membrane tubulating complex that in vitro can reconstitute the formation of membrane tubules with diameters similar to those observed in cellulo [42]. To be functional, ESCPE-1 forms a stable heterodimer of either SNX1 or SNX2 associated with either of SNX5 or SNX6, 2 additional BAR domain-containing orthologs [43]. Importantly, the mechanistic basis of how SNX27–Retromer delivers cargo into forming ESCPE-1 tubular profiles and tubulovesicular carriers remains a major unanswered question.

Here, we establish that a conserved surface in the FERM domain of SNX27 binds directly to acidic-Asp-Leu-Phe (aDLF) sequence motifs present in the disordered amino termini of the SNX1 and SNX2 subunits of ESCPE-1. We show that this interaction is required to handover PDZbm containing cargo proteins retrieved from lysosomal degradation by SNX27–Retromer into ESCPE-1 tubular profiles that promote cargo recycling for subsequent repopulation at the cell surface. Through evolutionary analysis of those protein–protein interactions that assemble

the SNX27:Retromer:ESCPE-1 coat complex, we reveal how this sorting axis has evolved to accommodate the increasing complexities of endosomal sorting observed in animals.

## Results

### The FERM domain of SNX27 promotes cargo recycling following SNX27–Retromer–mediated retrieval from lysosomal degradation

Previously, we have established that the interaction of Retromer with the PDZ domain of SNX27 is a crucial step in preventing the routing of internalized cargo into the lysosomal degradative pathway [13,14]. To identify the region(s) of SNX27 required for promoting subsequent cargo recycling to the plasma membrane, we used CRISPR gene editing to generate SNX27 knockout HeLa cells (Fig 1A). Compared to control cells, where endogenous GLUT1 was enriched at the cell surface, in the SNX27 knockout cells, GLUT1 displayed a steady-state enrichment with LAMP1-positive lysosomes, a phenotype that was also observed in a VPS35 knockout HeLa cell line (Fig 1B). Importantly, reexpression of GFP-SNX27 in the SNX27 knockout cells rescued the retrieval of GLUT1 from the lysosomal distribution and promoted its repopulation at the cell surface (Fig 1C). These data mirror those previously published using RNA interference (RNAi)-mediated SNX27 suppression [13] and confirm the SNX27 knockout HeLa cell line as a suitable screening platform through which to dissect the features of SNX27 required for promoting GLUT1 endosome-to-plasma membrane recycling.

In contrast to wild-type SNX27, expression of a SNX27 mutant lacking the loop region essential for Retromer association (GFP-SNX27Δ67–77) [13,14] failed to rescue retrieval from lysosomal colocalization and failed to promote GLUT1 cell surface recycling (Fig 1C). These data further confirm that the association of SNX27 with Retromer is a crucial step in coupling sequence-dependent cargo recognition with cargo retrieval from the lysosomal degradative fate [13,14]. Consistent with this, the expression of a SNX27 deletion mutant lacking the FERM domain (GFP-SNX27ΔFERM), a mutant that retained the association of SNX27 with Retromer, retained the ability to retrieve GLUT1 from lysosomes, as defined by a decreased colocalization between GLUT1 and LAMP1 (Fig 1C). However, the GFP-SNX27ΔFERM mutant failed to promote GLUT1 recycling to the cell surface, rather GLUT1 was enriched in a Retromer-positive endosomal compartment (Fig 1C). The overall levels of GLUT1 were not decreased in the KO and rescue conditions compared to parental cells (S1 Fig). Together, these data are consistent with a model in which the coupling of SNX27 to Retromer is necessary for retrieval from the lysosomal degradative fate, while the SNX27 FERM domain is required to promote the subsequent endosome-to-cell surface recycling of GLUT1.

### SNX1 and SNX2 couple ESCPE-1 to the FERM domain of SNX27

ESCPE-1 regulates tubular-based endosomal recycling of several cargos, many of which are also dependent on SNX27–Retromer [13,18,19]. ESCPE-1 is a heterodimeric assembly of the functionally redundant SNX1 or SNX2 associated with the functionally redundant SNX5 or SNX6 (Fig 2A) [18,19], while SNX27–Retromer is an assembly of SNX27 with the VPS26A/B:VPS35:VPS29 heterotrimeric Retromer complex (Fig 2B) [13]. To define a possible connection between SNX27 and ESCPE-1, we first performed a series of GFP-nanotrap immunoisolation of SNX27 and various SNX27 mutants expressed in HEK-293T cells and probed for the presence of associated endogenous ESCPE-1. Robust association was observed between full-length GFP-SNX27 and all components of ESCPE-1 (Fig 2C–2E). This association was independent of the SNX27 PDZ domain as binding was retained in the PDZ deletion mutant GFP-SNX27ΔPDZ and was not observed when just the PDZ domain was expressed in HEK-293T cells (Fig 2C and 2D).

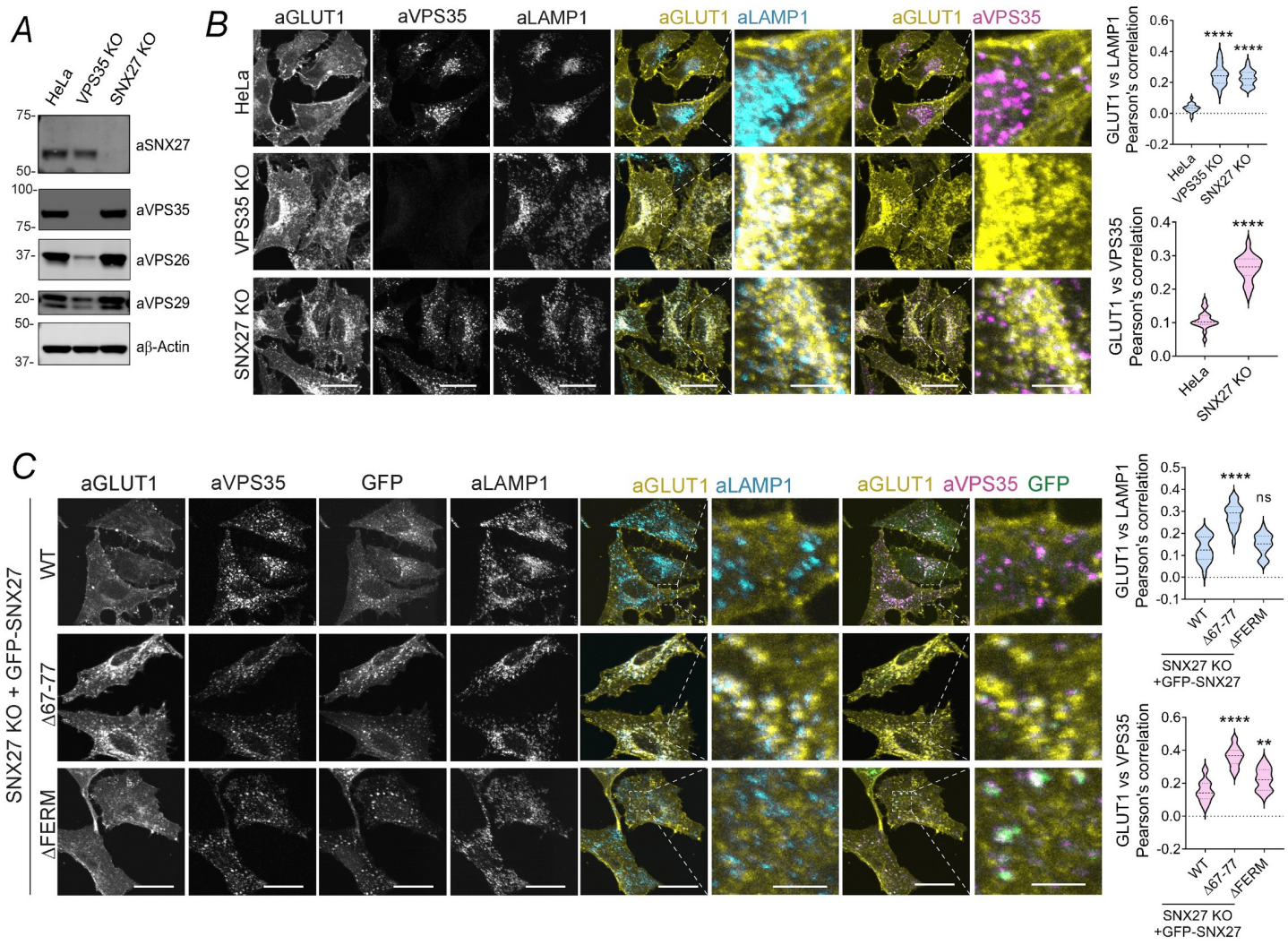


**Fig 1. The FERM domain of SNX27 promotes cargo recycling following SNX27–Retromer–mediated lysosomal retrieval. (A)** Western blot confirming the absence of the proteins of interest in VPS35 KO and SNX27 KO cells. **(B)** Representative images of parental Hela cells, VPS35 KO HeLa clonal line and SNX27 KO HeLa cells. The steady-state distribution of GLUT1 was analyzed by immunofluorescence staining of fixed cells with GLUT1 and the endosomal and lysosomal markers VPS35 and LAMP1. A total of 70 cells were analyzed in each condition for colocalization between GLUT1 and LAMP1 across $n = 4$ independent experiments. The Pearson coefficient values of LAMP1 colocalization were compared to the values of parental HeLa using 1-way ANOVA and Dunnett test: $P < 0.0001$ (HeLa vs VPS35 KO), $< 0.0001$ (HeLa versus SNX27 KO). Pearson coefficient values of VPS35 colocalization were compared using unpaired 2-tailed *t* test: $P < 0.0001$ (HeLa versus SNX27 KO). **(C)** Representative images of SNX27 KO HeLa cells transiently transfected with GFP-SNX27 WT, GFP-SNX27 Δ67–77 and GFP-SNX27 ΔFERM. Moreover, 48 hours after transfection, cells were fixed and immunostained. The steady-state distribution of GLUT1 was analyzed by immunofluorescence staining of fixed cells with GLUT1 and the endosomal and lysosomal markers VPS35 and LAMP1. A total of 70 cells were analyzed in each condition for colocalization between GLUT1 and LAMP1, and GLUT1 and VPS35 across $n = 4$ independent experiments. The Pearson coefficient values were compared to the values of SNX27 KO cells rescued with GFP-SNX27 WT using 1-way ANOVA and Dunnett test. LAMP1 colocalization values were $P < 0.0001$ (+WT versus +Δ67–77), 0.3559 (+WT versus +ΔFERM). VPS35 colocalization values were $P < 0.0001$ (+WT versus Δ67–77), 0.001 (+WT versus +ΔFERM). Bars, error bars, and symbols represent the mean, SEM, and individual data points, respectively. $^{*}P < 0.05$, $^{**}P < 0.01$, $^{***}P < 0.001$, $^{****}P < 0.0001$, ns = not significant. Scale bars, 25 μm (micrographs) and 5 μm (magnified images). The data underlying the graphs shown in the figure can be found in S1 Data. KO, knockout; SNX27, sorting nexin-27; WT, wild-type.

https://doi.org/10.1371/journal.pbio.3001601.g001

Retromer association with SNX27 was not required for ESCPE-1 binding as GFP-SNX27Δ67–77 and GFP-SNX27(L67A/L77A), 2 mutants that fail to bind to Retromer [14], each retained association with ESCPE-1 (Fig 2E). However, ESCPE-1 association was lost upon deletion of the SNX27 FERM domain (SNX27ΔFERM) or upon switching the FERM domain of SNX27 for the corresponding FERM domain from SNX17 (Fig 2C). Moreover, just the isolated FERM domain of SNX27, when expressed in HEK-293T cells, was able to associate with ESCPE-1 (Fig 2D).

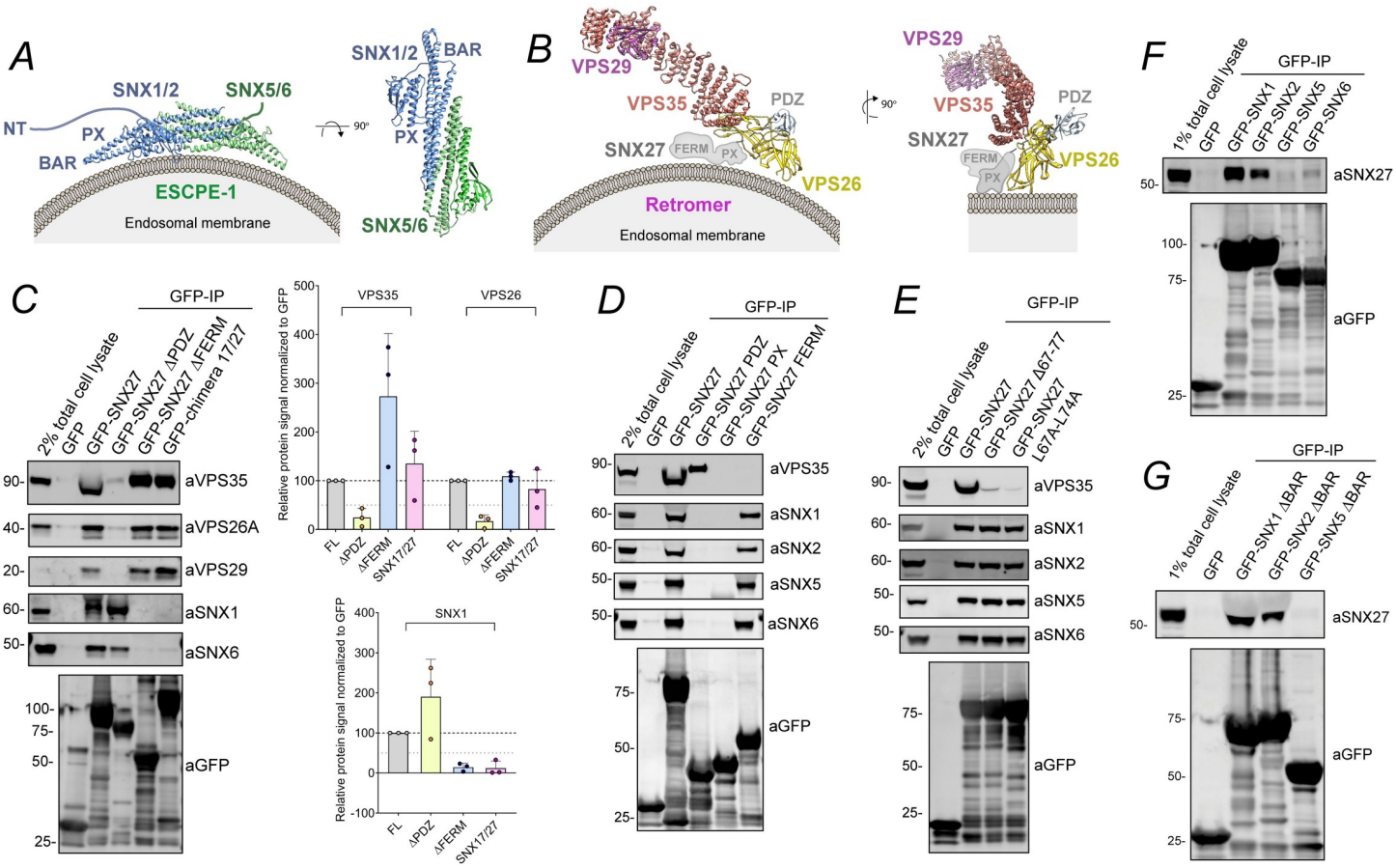


**Fig 2. The FERM domain of SNX27 interacts with SNX1 and SNX2. (A)** Schematics of ESCPE-1 assembly consisting of heterodimers of the SNX-BAR proteins SNX1 or SXN2 with SNX5 or SNX6. These SNXs have BAR and PX domains responsible of dimer formation and membrane targeting, respectively. SNX1 and SNX2 also have an extended amino-terminal unstructured extension (NT). **(B)** Schematics of the SNX27–Retromer assembly. Retromer is a stable heterotrimer of VPS35, VPS26, and VPS29. Retromer directly interacts with SNX27 through a β-hairpin insertion within the PDZ domain (residues 67 to 79) that engages a cleft of the VPS26 protein between the amino-terminal and carboxyl-terminal subdomains. **(C)** Co-immunoprecipitation of GFP-tagged SNX27 FL, SNX27 ΔPDZ, SNX27 ΔFERM and a chimera consisting of the SNX27 gene where its FERM domain was swapped for that of SNX17. The constructs were transiently transfected in HEK-293T cells, the cell lysates were subjected to GFP trap–based immunoprecipitation, and the immunoprecipitates were analyzed by quantitative fluorescence-based western blotting. The band intensities of VPS35, VPS26A, VPS29, SNX1, and GFP were measured from $n = 3$ independent experiments using Odyssey software. The band intensities, normalized to GFP expression, are presented as the average fraction of the FL. **(D)** Co-immunoprecipitation of GFP-tagged SNX27 FL, isolated SNX27 PDZ, PX, and FERM domains expressed in HEK-293T cells. The cell lysates were subjected to GFP trap–based immunoprecipitation, and the immunoprecipitates were blotted for VPS35, SNX1, SNX2, SNX5, SNX6, and GFP. The blot is representative of 3 independent GFP traps. **(E)** Co-immunoprecipitation of GFP-tagged SNX27 FL and the SNX27 mutants Δ67–77 and L67A-L74A expressed in HEK-293T cells. The cell lysates were subjected to GFP trap–based immunoprecipitation, and the immunoprecipitates were blotted for VPS35, SNX1, SNX2, SNX5, SNX6, and GFP. The blot is representative of 3 independent GFP traps. **(F)** Co-immunoprecipitation of GFP-tagged SNX1, SNX2, SNX5, and SNX6 expressed in HEK-293T cells. The cell lysates were subjected to GFP trap–based immunoprecipitation, and the immunoprecipitates were blotted for SNX27 and GFP. The blot is representative of 3 independent GFP traps. **(G)** Co-immunoprecipitation of GFP-tagged SNX1, SNX2, and SNX5 lacking the BAR domain (ΔBAR) expressed in HEK-293T cells. The cell lysates were subjected to GFP trap–based immunoprecipitation, and the immunoprecipitates were blotted for SNX27 and GFP. The blot is representative of 3 independent GFP traps. Molecular masses are given in kilodaltons. Bars, error bars, and symbols represent the mean, SEM, and individual data points, respectively. The data underlying the graphs shown in the figure can be found in S1 Data. ESCPE-1, endosomal SNX-BAR sorting complex for promoting exit 1; FL, full-length; SNX1, sorting nexin-1; SNX2, sorting nexin-2; SNX5, sorting nexin-5; SNX6, sorting nexin-6; SNX27, sorting nexin-27.

https://doi.org/10.1371/journal.pbio.3001601.g002

Finally, in the reverse immunoisolations, GFP-tagged SNX1, SNX2, SNX5, or SNX6 revealed that only SNX1 and SNX2 displayed a pronounced association with endogenous SNX27 when expressed in HEK-293T cells (Fig 2F). Moreover, this association did not require the presence of the SNX1 or SNX2 BAR domains, since deletion of these domains failed to affect binding to SNX27 (Fig 2G). Together, these data are consistent with the FERM domain of SNX27 associating with the SNX1 and SNX2 components of ESCPE-1.

## The amino termini of SNX1 and SNX2 present tandem acidic-Asp-Leu-Phe motifs that associate with the SNX27 FERM domain

Compared to SNX5 and SNX6, human SNX1 and SNX2 each contain amino-terminal extensions of 142 and 139 amino acids, respectively, which are predicted to be unstructured. Expression in HEK-293T cells of GFP-SNX1(1–279), a construct encoding for the amino-terminal extension plus the SNX1 PX domain, and GFP-SNX1(1–138), a construct encoding for just the amino-terminal extension of SNX1, established that the amino-terminal extension of SNX1 is sufficient for association with endogenous SNX27 (Fig 3A). Likewise, the amino terminus of SNX2 interacted with SNX27, while those of SNX5 and SNX6 failed to do so (S2A Fig). To establish the direct nature of the association, we recombinantly expressed and purified full-length mouse SNX1 and the isolated FERM domain of human SNX27; mouse and human SNX1 are 94.2% identical. Isothermal titration calorimetry (ITC) established that SNX1 bound directly to the FERM domain of SNX27 with an affinity ($K_d$) of 41.0 μM (Fig 3B and S1 Table). A similar binding affinity (39.1 μM) was observed with a recombinant protein corresponding to the amino-terminal extension of mouse SNX1 (85.9% sequence identity with human SNX1) (Fig 3B). To map down the features of SNX1 and SNX2 required for SNX27 binding, we performed a deletion mutagenesis screen of the amino-terminal extension of human SNX1 (Fig 3C). Walking upstream from a minimal binding region encoded by residues 1 to 138 established that 2 regions were required for maximal SNX27 binding. Deletion of residues 79 to 100 led to a pronounced reduction in binding and subsequent deletion of residues 41 to 54 abolished the interaction. Alignment of these regions of SNX1 revealed 2 similar motifs with DIF or DLF sequences flanked by upstream acidic residues. Comparison with the amino terminus of SNX2, which also binds SNX27 (S2A Fig), showed that it also has 2 similar sequences in its disordered amino-terminal domains, and, altogether, these define a conserved sequence D/E-x-x-D-I/L-F, here termed the aDLF motif (Fig 3D and 3E).

Site-directed mutagenesis targeting the first aDLF motif of SNX1 established that full-length GFP-SNX1(E42K), GFP-SNX1(E44K), GFP-SNX1(D45K), GFP-SNX1(I46K), and GFP-SNX1 (F47K) all displayed reduced binding to SNX27 of around 50% (Fig 3F). A similar reduction in binding was also observed when targeting the second aDLF motif of SNX1 as observed with the GFP-SNX1(E84K), GFP-SNX1(D87K), and GFP-SNX1(F89D) mutants (Fig 3F). In a double GFP-SNX1(D45K,D87K) mutant that simultaneously targeted key residues in both aDLF motifs SNX27, binding was reduced to near undetectable levels (Fig 3F). Importantly, all mutants retained their ability to associate with SNX6, establishing that ESCPE-1 was still able to assemble. In addition, the mutant targeting both aDLF motifs in SNX2, GFP-SNX2(D26K,D72K), also reduced SNX27 binding to near undetectable levels (S2B Fig). Next, we used ITC to quantify the binding of aDLF peptides from SNX1 and SNX2 to full-length mouse SNX27. Peptides corresponding to residues 35 to 51 and 75 to 92 encompassing the first and second aDLF motifs of human SNX1, respectively, bound to SNX27 with respective affinities of 33.4 μM and 13.3 μM (Fig 3G and S1 Table). Establishing the redundant nature of the interaction with SNX27, we designed peptides corresponding to the first and second aDLF motifs of SNX2, namely residues 16 to 33 and 62 to 82. These also bound to full-length mouse SNX27 with affinities of 37.8 μM and 22.6 μM, respectively (Fig 3H). Further defining the redundancy between SNX1 and SNX2, introduction of a charge swap mutation into the SNX1 35–51 peptide, SNX1 (D45K), and a triple mutation in the SNX2 16–33 peptide, SNX2(DLF-SSS), resulted in mutant peptides that showed no detectable binding to SNX27 (Fig 3G and 3H). Finally, a competitive ITC assay using full-length SNX27 preincubated with excess SNX1 75–92 peptide established that it competed for binding of SNX2 16–33 peptide, consistent with both sequences associating with the same surface within the SNX27 FERM domain (S2C Fig). Overall, these data establish

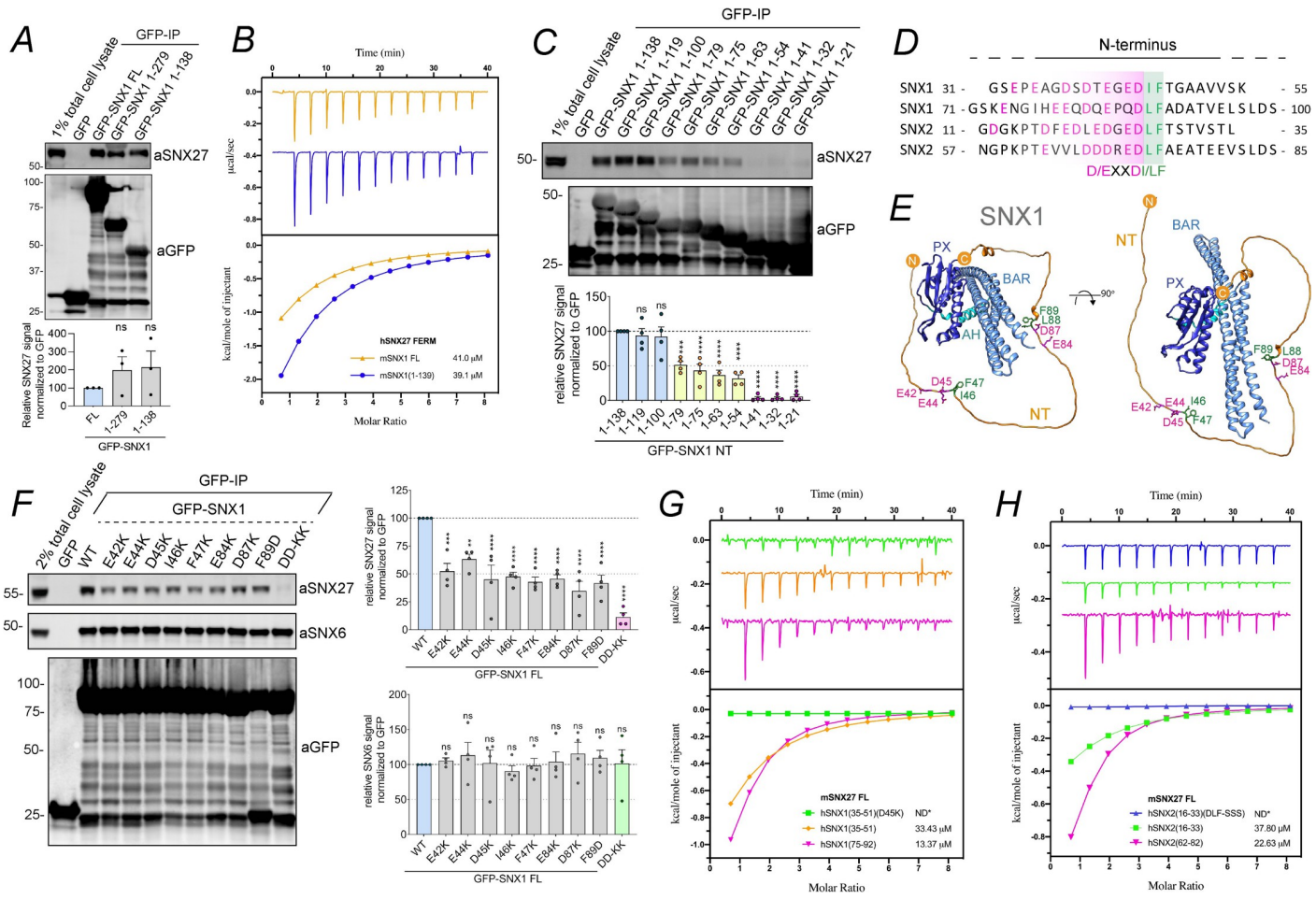


**Fig 3. The amino termini of SNX1 and SNX2 directly interact with SNX27 FERM domain through tandem aDLF motifs. (A)** Co-immunoprecipitation of GFP-tagged SNX1 FL or truncation mutants corresponding to residues 1 to 279 and 1 to 138 expressed in HEK-293T cells. The cell lysates were subjected to GFP trap–based immunoprecipitation, and the immunoprecipitates were blotted for SNX27 and GFP. The band intensity of SNX27 was measured from $n = 3$ independent experiments using Odyssey software and was normalized to GFP expression. The relative binding of SNX1 constructs was compared with the SNX1 FL using a 1-way ANOVA and Dunnett test. **(B)** Binding of $mSNX1_{FL}$ (orange) and $mSNX1_{1-139}$ (blue) with $hSNX27_{FERM}$ by ITC. **(C)** Co-immunoprecipitation of GFP-tagged SNX1 amino terminus (1 to 138) and a panel of constructs corresponding to serial truncations of SNX1 amino terminus. The constructs were transiently transfected in HEK-293T cells, the cell lysates were subjected to GFP trap–based immunoprecipitation, and the immunoprecipitates were analyzed by quantitative fluorescence-based western blotting. The band intensity of SNX27 and GFP was measured from $n = 4$ independent experiments using Odyssey software and was normalized to GFP expression. The relative binding of SNX1 truncation mutants was compared with the SNX1 amino terminus (1–138) using a 1-way ANOVA and Dunnett test. **(D)** Alignment of the SNX1 regions that are involved in SNX27 binding with the corresponding sequences in the SNX2 amino terminus. The conserved residues between SNX1 and SNX2 account for a consensus motif of acidic residues followed by DI/LF (aDLF motif). **(E)** Alphafold structural prediction for FL SNX1 [44]. The amino terminus of SNX1 is shown in its full extension and the residues involved in SNX27 binding are colored in red and green. **(F)** Co-immunoprecipitation of GFP-tagged SNX1 WT and a panel of amino acid swap mutants across the aDLF motifs of SNX1. The constructs were transiently transfected in HEK293T cells, the cell lysates were subjected to GFP trap–based immunoprecipitation, and the immunoprecipitates were analyzed by quantitative fluorescence-based western blotting. The band intensities of SNX27, SNX6, and GFP were measured from $n = 4$ independent experiments using Odyssey software. The band intensity, normalized to GFP expression, is presented as the average fraction of SNX1 WT. The binding of SNX1 point mutants to SNX27 and SNX6 were compared with the SNX1 WT using a 1-way ANOVA and Dunnett test. **(G)** Binding of $mSNX27_{FL}$ and hSNX1 peptides by ITC. $SNX1_{35-51(D45K)}$: green; $SNX1_{35-51}$: orange; $SNX1_{75-92}$: lilac; ND*: no binding detected. **(H)** Binding of $mSNX27_{FL}$ and hSNX2 peptides by ITC. $SNX2_{16-33(DLF/SSS)}$: blue; $SNX2_{16-33}$: green; $SNX2_{62-82}$: lilac; ND*: no binding detected. The ITC graphs represent the integrated and normalized data fit with 1:1 ratio binding. The binding affinity ($K_d$) is given as mean of at least 2 independent experiments. Thermodynamic parameters for the binding are provided in S1 Table. Molecular masses are given in kilodaltons. Bars, error bars, and symbols represent the mean, SEM, and individual data points, respectively. $^{*}P < 0.05$, $^{**}P < 0.01$, $^{***}P < 0.001$, $^{****}P < 0.0001$. The data underlying the graphs shown in the figure can be found in S1 Data. aDLF, acidic-Asp-Leu-Phe; FL, full-length; ITC, isothermal titration calorimetry; SNX1, sorting nexin-1; SNX2, sorting nexin-2; SNX27, sorting nexin-27; WT, wild-type.

https://doi.org/10.1371/journal.pbio.3001601.g003

that through tandem aDLF motifs present within their unstructured amino terminal extensions SNX1 and SNX2 directly associate with the FERM domain of SNX27.

## A basic surface in the SNX27 FERM domain is required for SNX1/SNX2 binding

SNX27 and SNX17 are related endosome associated cargo adaptors [23,45]. While they display entirely distinct functional roles in sequence-dependent endosomal cargo sorting [13,15], they share structurally similar PX and FERM domains [45,46] (Fig 4A). A comparative immunoisolation of GFP-SNX17 and GFP-SNX27 from HEK-293T cells established that SNX17 does not bind to ESCPE-1 (Fig 4B), consistent with the loss of ESCPE-1 binding to the SNX27 chimera containing the SNX17 FERM domain (Fig 2C). To identify potential regions for aDLF motif binding to the SNX27 FERM domain, we initially performed a comparative structural analysis between the X-ray structure of the SNX17 FERM domain [45] and a homology model of the SNX27 FERM domain [46]. In particular, we focused on the distribution and clustering of complementary basic amino acids. This revealed that the FERM domain of SNX27 possesses a basic surface defined in part by R437, R438, K495, K496, R498, and K501, residues that in SNX17 often corresponded to uncharged residues or negatively charged amino acids (Fig 4A and 4C). Indeed, charge swap site-directed mutagenesis of these residues generated full-length GFP-SNX27 mutants that when expressed and immunoisolated from HEK-293T cells lacked the ability to associate with ESCPE-1; all mutants, however, retained the ability to associate with Retromer (Fig 4D). In direct ITC-quantified binding assays human SNX27(K495D), SNX27(R498D), and SNX27(K501D) all displayed no detectable binding to the human SNX1 75–92 peptide, while the SNX27(R496D) mutant displayed a reduce binding affinity of 56.4 μM when compared with the 12.7 μM observed for wild-type SNX27 (Fig 4E).

Finally, we modeled the binding of the aDLF sequences from SNX1 and SNX2 with SNX27 using the AlphaFold2 machine learning algorithm [47,48]. In total, we generated 12 models, with 3 models each of SNX27 in the presence of the 4 separate aDLF peptides (Figs 4F and S3A–S3C). Without any prior inputs apart from the SNX27 and peptide sequences, AlphaFold2 produced very high confidence models of the SNX27 FERM domain. Remarkably, in all 12 models, the aDLF peptides associated specifically with the SNX27 F3 subdomain, near the basic surface identified by mutagenesis (Fig 4F). Closer inspection showed that in 8 of the models the core D[L/I]F residues adopted essentially identical bound structures, with the hydrophobic [L/I]F side chains inserting into a hydrophobic pocket and interacting with SNX27 I467, F469, Y490, and V500 and the acidic Asp side chain surrounded by the complementary basic SNX27 residues R437, R438, K439, and R498 (Fig 4F). To further validate the model, we therefore mutated I467, Y490, and V500 to Lys, all of which disrupted the interaction of SNX27 with ESCPE-1 (Fig 4G). Together, these models are entirely consistent and strongly support the mutagenesis data for the SNX27-peptide interactions.

## SNX27 association with ESCPE-1 couples cargo retrieval with promotion of cell surface recycling

To define the functional significance of the association of SNX27 to ESCPE-1, we first transfected our SNX27 knockout HeLa cells line with constructs encoding for either GFP-tagged wild-type SNX27 or the ESCPE-1 binding defective mutant GFP-SNX27(R498D) (Fig 5A). Analysis of their relative subcellular distributions established that they each associated with EEA1 and SNX6-positive endosomes (Fig 5B). Previously, we established that by binding to the PDZbm present within the cytoplasmic facing tail of GLUT1, the SNX27–Retromer complex serves to retrieve internalized GLUT1 away from lysosomal mediated degradation ([13], and see Fig 1A). We therefore performed a series of rescue experiments to quantify the SNX27-dependent retrieval of internalized GLUT1 from lysosomal mediated degradation, using the SNX17–Retriever-mediated retrieval of alpha-5 integrin as a negative control (Fig

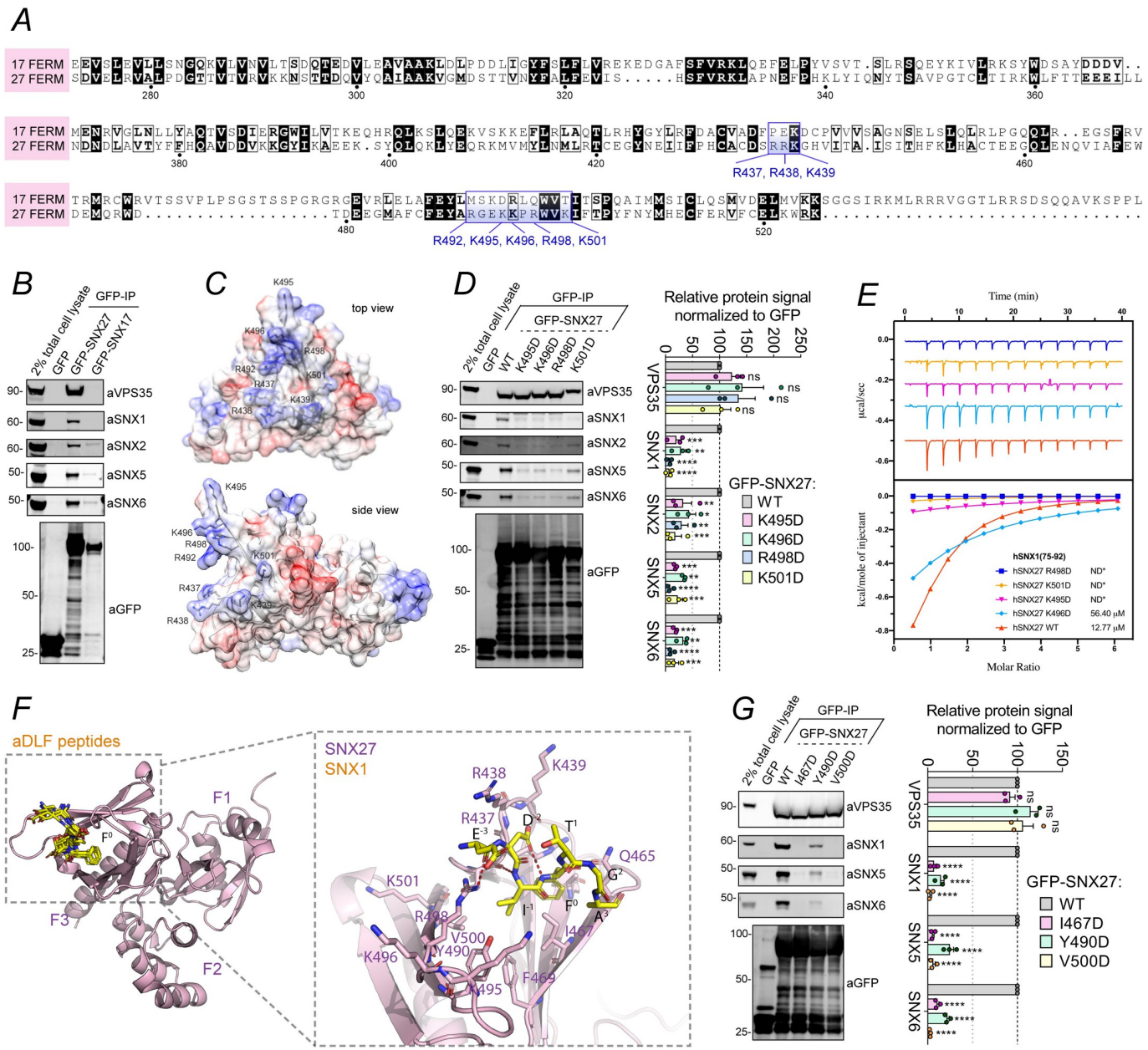


**Fig 4. SNX1 and SNX2 amino termini bind a unique basic surface of the SNX27-FERM domain. (A)** Sequence alignment of SNX27 FERM domain with the SNX17 FERM domain. The positively charged residues that constitute a basic surface unique to SNX27 are boxed and labeled in blue. **(B)** Co-immunoprecipitation of GFP-tagged SNX27 and SNX17. The constructs were transiently transfected in HEK-293T cells, the cell lysates were subjected to GFP trap–based immunoprecipitation, and the immunoprecipitates were blotted for VPS35, SNX1, SNX2, SNX5, SNX6, and GFP. The blot is representative of 3 independent GFP traps. **(C)** Homology model of the SNX27 FERM domain [46]. The residues that are unique to SNX27 FERM domain and those that may account for the interaction with ESCPE-1 are labeled. **(D)** Co-immunoprecipitation of GFP-tagged SNX27 WT and a panel of amino acid swap mutants across the FERM domain. The constructs were transiently transfected in HEK293T cells, the cell lysates were subjected to GFP trap–based immunoprecipitation, and the immunoprecipitates were blotted for VPS35, SNX1, SNX2, SNX5, and SNX6. The band intensities were measured from $n = 3$ independent experiments using Odyssey software. The band intensity, normalized to GFP expression, is presented as the average fraction of the WT. The binding of SNX27 point mutants to VPS35, SNX1, SNX2, SNX5, and SNX6 was compared with the SNX27 WT using a 2-way ANOVA and Dunnett test. **(E)** Binding of $SNX1_{75\text{-}92}$ peptide to $hSNX27_{FL}$ proteins by ITC (hSNX27 R498D: dark-blue; hSNX27 K501D: orange; hSNX27 K495D: lilac; hSNX27 K496D: sky-blue; hSNX27 WT: red-orange; ND*: no binding detected). The ITC graphs represent the integrated and normalized data fit with 1:1 ratio binding. The binding affinity ($K_d$) is given as mean of at least 2 independent experiments. Thermodynamic parameters for the binding are provided in S1 Table. **(F)** The left panel shows the AlphaFold2 generated model of the SNX27 FERM domain (pink ribbons) bound to the core aDLF sequences (yellow sticks) of SNX1 and SNX2 with identical binding orientations. For clarity, only one SNX27 model is shown with the 8 aDLF peptides overlaid (2 peptide models each of the 4 sequences from SNX1 and SNX2). The 3 subdomains of the SNX27 FERM domain F1, F2, and F3 are indicated. The middle panel shows a close-up view of the modeled SNX1 aDLF core sequence $^{44}$EDIFTGA$^{50}$. The strictly conserved Phe side chain of the aDLF sequences is numbered $F^0$ for reference, and other residues are numbered with respect to this. **(G)** Co-immunoprecipitation of GFP-tagged SNX27 and a panel of

hydrophobic amino acid mutations predicted to mediate the SNX27 FERM–ESCPE1 binding. The constructs were transiently transfected in HEK-293T cells, the cell lysates were subjected to GFP trap–based immunoprecipitation, and the immunoprecipitates were blotted for VPS35, SNX1, SNX5, SNX6, and GFP. The blot is representative of 3 independent GFP traps with the normalized enrichment of SNX27 association relative to expression of GFP-tagged protein quantified in the bar chart. Molecular masses are given in kilodaltons. Bars, error bars, and symbols represent the mean, SEM, and individual data points, respectively. $^{*}P < 0.05$, $^{**}P < 0.01$, $^{***}P < 0.001$, $^{****}P < 0.0001$. The data underlying the graphs shown in the figure can be found in S1 Data. aDLF, acidic-Asp-Leu-Phe; ESCPE-1, endosomal SNX-BAR sorting complex for promoting exit 1; ITC, isothermal titration calorimetry; SNX1, sorting nexin-1; SNX2, sorting nexin-2; SNX5, sorting nexin-5; SNX6, sorting nexin-6; SNX27, sorting nexin-27; WT, wild-type.

https://doi.org/10.1371/journal.pbio.3001601.g004

5C) [15]. In the SNX27 knockout HeLa cells, GLUT1 displayed an enhanced rate of degradation following 8 hours of treatment with cycloheximide, data that are consistent with the loss of SNX27 expression leading to a reduced ability for transporter retrieval from the lysosomal degradative fate (Fig 5C). This phenotype was rescued by reexpression of wild-type GFP-tagged SNX27 (Fig 5C). Interestingly, expression of GFP-SNX27(R498D), a mutant that fails to associate with ESCPE-1 but retains binding to Retromer (Fig 4D and 4E), also fully rescued the retrieval of GLUT1 from lysosomal degradation (Fig 5C). The coupling of SNX27–Retromer to the ESCPE-1 complex is therefore not required for the retrieval of GLUT1 from lysosomal degradation.

Next, we turned to examining the promotion of GLUT1 recycling back to the cell surface. Here, we utilized restricted cell surface biotinylation to quantify the amount of GLUT1 at the cell surface [13]. Compared with control HeLa cells, SNX27 knockout HeLa cells displayed a reduced cell surface abundance of GLUT1, a result of missorting of internalized GLUT1 for lysosomal degradation (Fig 5D). Again, this phenotype was rescued by expression of GFP-SNX27 (Fig 5D) [13]. In contrast, expression of GFP-SNX27(R498D) failed to rescue the cell surface level of GLUT1 (Fig 5D), consistent with the association of SNX27 with ESCPE-1 being required to promote the cell surface recycling of internalized GLUT1. Importantly, GFP-SNX27(R498D) exhibited an endosomal localization indistinguishable from wild-type SNX27 (Fig 5B), consistent with the inability to promote endosome-to-plasma membrane recycling of GLUT1 not arising from a loss of endosomal localization. Furthermore, confocal analysis of the steady-state distribution of GLUT1 in GFP-SNX27(R498D) rescue cells confirmed that GLUT1 was retrieved from the lysosomal degradative fate, as shown by reduced co-localization with the LAMP1-labeled lysosome (Fig 5E). However, unlike the rescue with wild-type GFP-SNX27, where GLUT1 was enriched at the cell surface, the GLUT1 in the GFP-SNX27(R498D) rescue displayed an increased level of intracellular puncta and failed to repopulate the cell surface suggestive of the transporter being trapped in an endosomal compartment (Fig 5E), the precise nature of which will require further study. Together, these data are consistent with SNX27 orchestrating cargo retrieval from the degradative fate through its PDZ domain-mediated association with cargo and Retromer, while the SNX27 FERM domain mediates association with ESCPE-1 to promote tubular-based plasma membrane recycling of the retrieved cargo.

## ESCPE-1 association with SNX27 couples cargo retrieval with promotion of cell surface recycling

To complete the mechanistic dissection of SNX27 coupling to ESCPE-1, we used a previously characterized double SNX1 and SNX2 knockout HeLa cell line [49] to generate lentiviral transduced stable lines expressing GFP-SNX1 or GFP-SNX1(D45K,D87K) (Fig 6A). When expressed at near to endogenous levels each chimera displayed an indistinguishable association with EEA1 and SNX6-labeled endosomes (Fig 6B). Consistent with ESCPE-1 not being required for GLUT1 retrieval from lysosomal degradation, the rate of internalized GLUT1 degradation following 8 hours of treatment with cycloheximide was equivalent between

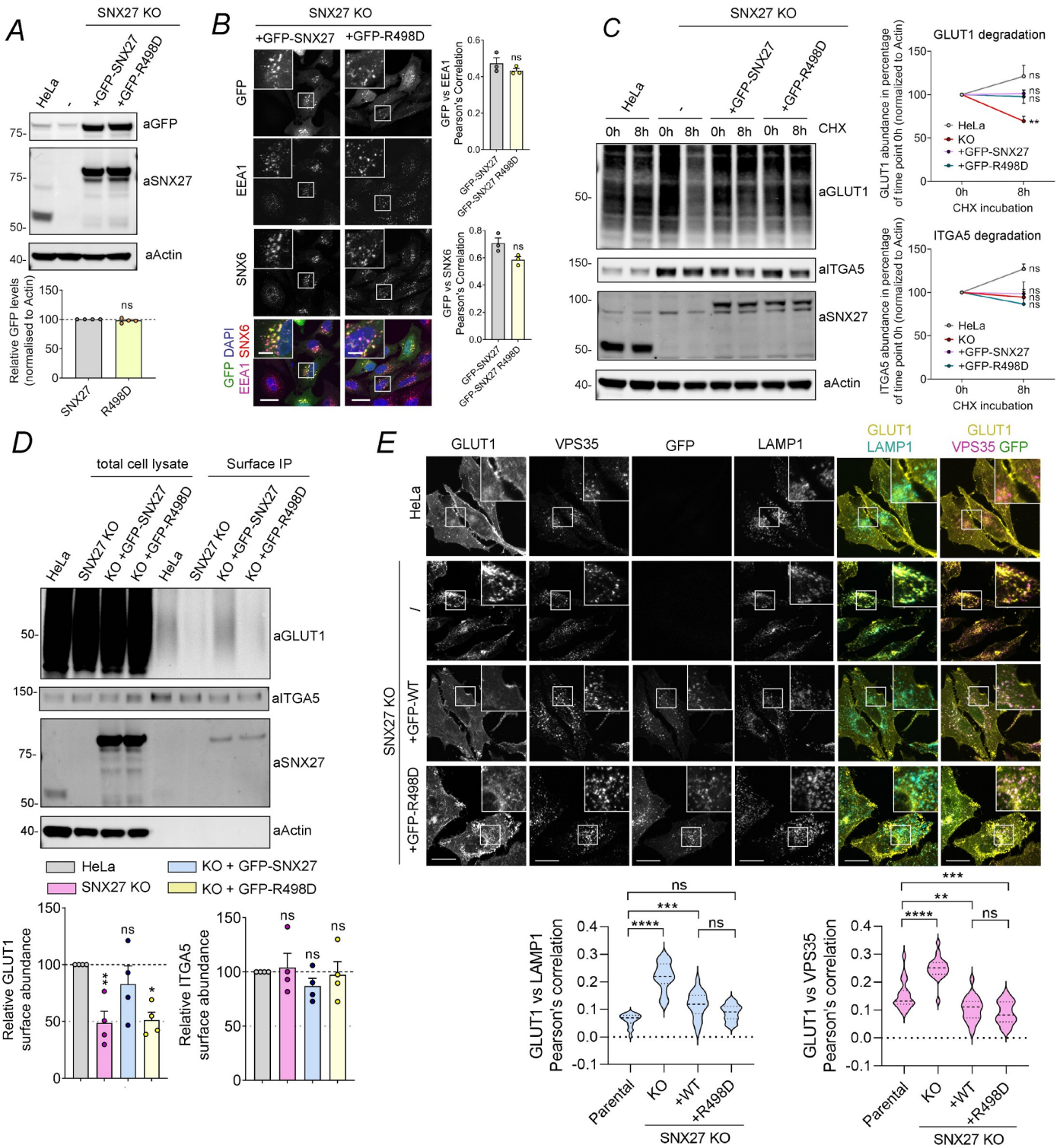


**Fig 5. SNX27:ESCPE-1 interaction is required for endosome-to-plasma membrane recycling of SNX27 cargos. (A)** Representative western blot showing similar expression levels between transiently expressed GFP-SNX27 and GFP-SNX27(R498D). **(B)** Representative images of SNX27 KO HeLa cells transiently transfected with GFP-SNX27 or GFP-SNX27(R498D). Moreover, 48 hours after transfection, cells were fixed and immunostained for the endosomal markers EEA1 and SNX6. Magnified views of the white boxes are shown boxed. Cell numbers analyzed for colocalization were 60 GFP–SNX27 and 60 GFP–SNX27 R498D cells across $n = 3$ independent experiments. The Pearson coefficient values were compared using a 2-tailed unpaired $t$ test; for EEA1 $P = 0.2971$, SNX6 $P = 0.0506$. **(C)** Degradation assay in parental HeLa cells or SNX27 KO HeLa cells that were transiently transfected with GFP-SNX27 or GFP-SNX27(R498D) mutant. Moreover, 48 hours after transfection, cells were incubated with 10 μg/ml cycloheximide and lysed at different time points as indicated. The band intensities of endogenous GLUT1 and

ITGA5 were measured from $n = 3$ independent experiments using Odyssey software. The levels of GLUT1 and ITGA5 at 8 hours were compared with the corresponding level at 0-hour time point. Analysis was done using a 2-way ANOVA and Sidak test. GLUT1: $P = 0.0735$ (HeLa), 0.0068 (KO), 0.9997 (+GFP-SNX27), 0.9975 (+GFP-R498D). ITGA5: $P = 0.1151$ (HeLa), 0.9820 (KO), 0.9999 (+GFP-SNX27), and 0.6899 (+GFP-R498D). **(D)** Analysis of surface levels of GLUT1 and ITGA5 in parental HeLa cells or SNX27 KO HeLa cells that were transiently transfected with GFP-SNX27 or GFP-SNX27(R498D) mutant. Moreover, 48 hours after transfection, cells were subjected to surface biotinylation followed by streptavidin-based immunoisolation. The immunoisolates were blotted for GLUT1, and the band intensities were measured from $n = 4$ independent experiments using Odyssey software and compared to the levels in parental HeLa using 1-way ANOVA and Dunnett test. GLUT1: $P = 0.0134$ (KO versus HeLa), 0.9587 (+GFP-SNX27 versus HeLa), and 0.0163 (+GFP-SNX27 R498D versus HeLa). The immunoisolates were blotted for ITGA5, and the band intensities were measured from $n = 3$ independent experiments using Odyssey software and compared to the levels in parental HeLa using 1-way ANOVA and Dunnett test. ITGA5: $P = 0.5616$ (KO versus HeLa), 0.0733 (+GFP-SNX27 versus HeLa), and 0.2354 (+GFP-SNX27 R498D versus HeLa). **(E)** Representative images of parental Hela cells, SNX27 KO HeLa cells transiently transfected with GFP-SNX27 or GFP-SNX27(R498D). Moreover, 48 hours after transfection, cells were fixed and immunostained for the cargo GLUT1, the endosomal marker VPS35, and the late endosome/lysosome marker LAMP1. A total of 60 cells were quantified per condition in $n = 4$. The Pearson coefficient values were compared to the values of Parental HeLa using 1-way ANOVA and Dunnett test. The values for LAMP1 colocalization were $P < 0.0001$ (Parental versus KO), 0.0001 (Parental versus +WT), 0.1084 (Parental versus +R498D), <0.0001 (+WT versus KO), and 0.0692 (+WT versus +R498D). The values for VPS35 colocalization were $P < 0.0001$ (Parental versus KO), 0.0029 (Parental versus +WT), 0.0001 (Parental versus +R498D), <0.0001 (+WT versus KO), and 0.6346 (+WT versus +R498D). Scale bars, 25 μm (micrographs) and 5 μm (magnified images). Molecular masses are given in kilodaltons. Bars, error bars, and symbols represent the mean, SEM, and individual data points, respectively. $^{*}P < 0.05$, $^{**}P < 0.01$, $^{***}P < 0.001$, $^{****}P < 0.0001$, ns = not significant. The data underlying the graphs shown in the figure can be found in S1 Data. ESCPE-1, endosomal SNX-BAR sorting complex for promoting exit 1; KO, knockout; SNX6, sorting nexin-6; SNX27, sorting nexin-27; WT, wild-type.

https://doi.org/10.1371/journal.pbio.3001601.g005

parental HeLa cells, the SNX1/SNX2 knockout cells, and the GFP-SNX1 and GFP-SNX1 (D45K,D87K) rescue lines (Fig 6C). In contrast, the quantification of restricted cell surface biotinylation established that compared to the parental HeLa cells, the SNX1/SNX2 double knockout HeLa cells displayed a reduced cell surface abundance of GLUT1 consistent with a defect in recycling of internalized GLUT1 (Fig 6D). While reexpression of GFP-SNX1 rescued the cell surface level of GLUT1, expression of the GFP-SNX1(D45K,D87K) mutant, defective in SNX27 association (Fig 3F), failed to rescue the cell surface recycling of GLUT1 (Fig 6D). Finally, confocal analysis of the steady-state distribution of GLUT1 revealed that when compared to parental cells, the glucose transporter was enriched in Retromer decorated endosomes in the SNX1/SNX2 double knockout HeLa cells (Fig 6E), in agreement with GFP-SNX27ΔFERM rescue (see Fig 1C). Reexpression of GFP-SNX1 partially rescued the cell surface delivery of GLUT1 from this compartment, while expression of GFP-SNX1(D45K, D87K) showed an increase in colocalization of GLUT1 with Retromer decorated endosomes (Fig 6E). Taken together, these data provide an independent validation that the association of ESCPE-1 to the FERM domain of SNX27 is required to promote tubular-based endosomal exit and cell surface recycling of cargo retrieved from lysosomal degradation.

## Evolutionary assembly of the SNX27:Retromer:ESCPE-1 sorting axis

We used phylogenetic analyses to investigate the evolution of the association of SNX27 with Retromer and with the ESCPE-1 complex. The inferred phylogeny of SNX27 suggests the gene was ancestrally present in filozoans (i.e., the group comprising filastereans, choanoflagellates, and metazoans) (S4A Fig). In SNX27, an exposed ß-hairpin in the SNX27 PDZ domain, encoded by residues 67 to 79 in human SNX27, engages a groove in the VPS26A (and VPS26B) subunit of Retromer [14] (Fig 7A). An equivalent sequence, including key residues Leu-67 and Leu-74 of the ß-hairpin, is present in SNX27 across all choanozoans (this is, the group comprising metazoans and choanoflagellates; Figs 7B and S4A). Key residues in VPS26A required for SNX27 binding include D44 and L154, equivalent residues in VPS26B being D42 and L152 [14]. The inferred phylogeny of VPS26A and VPS26B revealed that VPS26B is ancestrally present across eukaryotes, with a duplication of VPS26B in vertebrates leading to the emergence of VPS26A (Figs 7B and S4B). Interestingly, within VPS26B, the D44 residue is present ancestrally in filozoans, while the L154 residue evolved in choanozoans (Fig 7B). Together, these analyses suggest that the SNX27–Retromer association first appeared in the last common ancestor of choanoflagellates and metazoans.

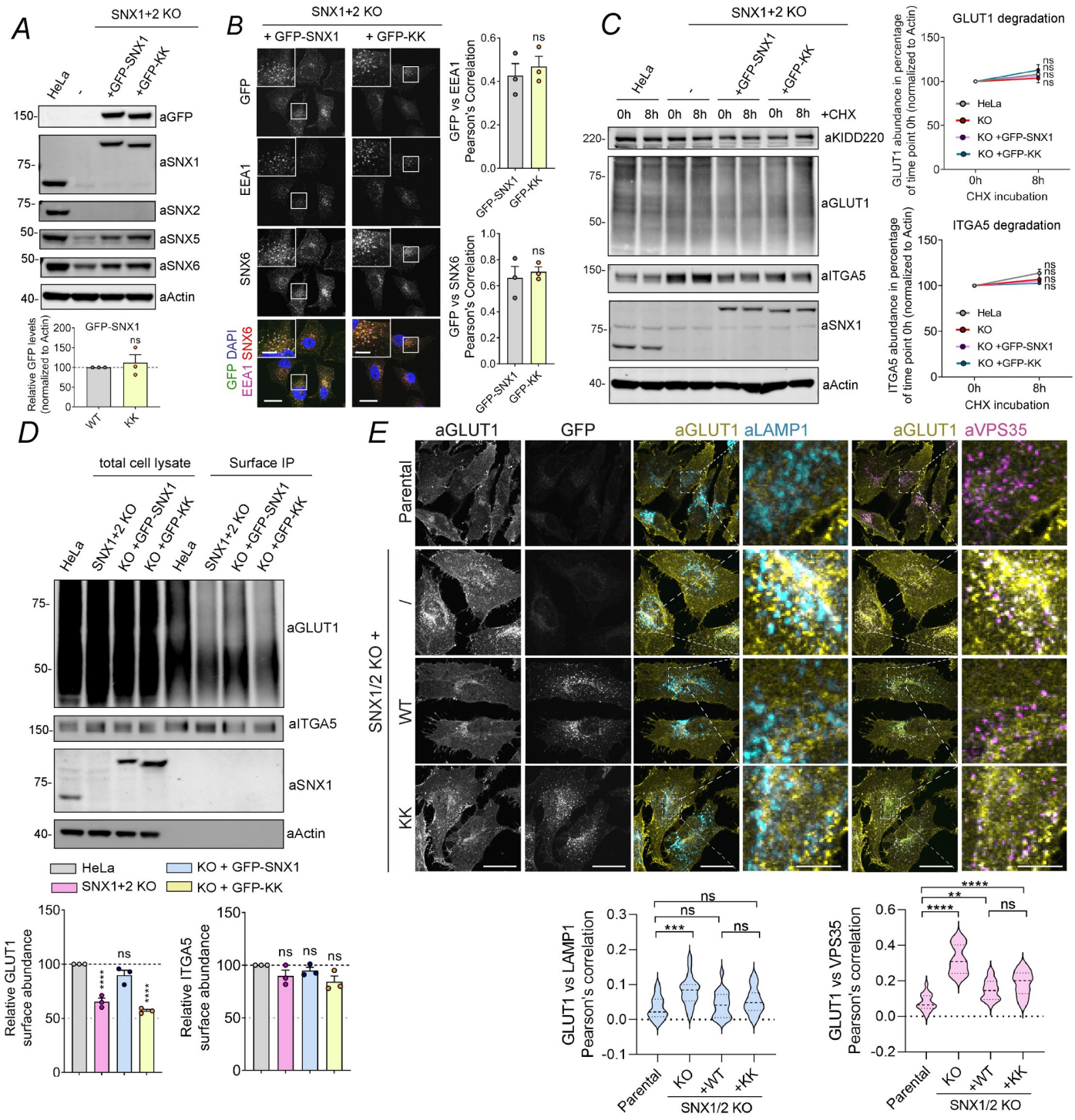


**Fig 6. ESCPE-1 interaction with SNX27 is required for endosome-to-plasma membrane recycling of GLUT1. (A)** Representative western blot showing similar expression levels between stably transfected GFP-SNX1 and GFP-SNX1(KK) in SNX1/2KO cells. SNX1 band intensities were measured from $n = 3$ and normalized to actin. Analysis was done using a 2-tailed unpaired $t$ test. **(B)** Representative images of SNX1/2 KO HeLa cell line stably transfected with GFP-SNX1 or GFP-SNX1 (KK). Cells were fixed and immunostained for the endosomal markers EEA1 and SNX6. Magnified views of the white boxes are shown boxed. Cell numbers analyzed for colocalization were 50 GFP–SNX1 and 50 GFP–SNX1(KK) cells across $n = 3$ independent experiments. The Pearson coefficient values were compared using a 2-tailed unpaired $t$ test; for EEA1 $P = 0.5971$, SNX6 $P = 0.6459$. **(C)** Degradation assay in parental HeLa cells or SNX1/2 KO HeLa cells that were stably transfected with GFP-SNX1 or GFP-SNX1(KK) mutant. Cells were incubated with 10 μg/ml cycloheximide and lysed at different time points as indicated. The band intensities of endogenous GLUT1 and ITGA5 were measured from $n = 3$ independent experiments using Odyssey software. The levels of GLUT1 and ITGA5 at 8 hours were compared with the corresponding level at 0-hour time point. Analysis was done using a 2-way ANOVA and Sidak test. GLUT1: $P = 0.6796$ (HeLa),

0.9768 (KO), 0.8430 (+GFP-SNX1), and 0.2665 (+GFP-KK). ITGA5: $P = 0.2247$ (HeLa), 0.7892 (KO), 0.9196 (+GFP-SNX1), and 0.9930 (+GFP-KK). **(D)** Analysis of surface levels of GLUT1 and ITGA5 in parental HeLa cells or SNX1/2 KO HeLa cells that were stably transfected with GFP-SNX1 or GFP-SNX1(KK) mutant. Cells were subjected to surface biotinylation followed by streptavidin-based immunoisolation. The immunoisolates were blotted for GLUT1, and the band intensities were measured from $n = 3$ independent experiments using Odyssey software and compared to the levels in parental HeLa using 1-way ANOVA and Dunnett test. GLUT1: $P = <0.0001$ (KO versus HeLa), 0.0878 (+GFP-SNX1 versus HeLa), and <0.0001 (+GFP-KK versus HeLa). The immunoisolates were blotted for ITGA5, and the band intensities were measured from $n = 3$ independent experiments using Odyssey software and compared to the levels in parental HeLa using 1-way ANOVA and Dunnett test. ITGA5: $P = 0.2592$ (KO versus HeLa), 0.7185 (+GFP-SNX1 versus HeLa), and 0.0653 (+GFP-KK versus HeLa). **(E)** Representative images of parental Hela cells, SNX1/2 KO HeLa cells stably transfected with GFP-SNX1 or GFP-SNX1(KK). Cells were fixed and immunostained for the cargo GLUT1, the endosomal marker VPS35, and the late endosome/lysosome marker LAMP1. A total of 50 cells were quantified per condition in $n = 3$. The Pearson coefficient values were compared to the values of Parental HeLa using 1-way ANOVA and Dunnett test. The values for LAMP1 colocalization were $P = 0.0002$ (Parental versus KO), 0.7919 (Parental versus +WT), 0.2225 (Parental versus +KK), 0.0028 (+WT versus KO), and 0.6677 (+WT versus +KK). The values for VPS35 colocalization were <0.0001 (Parental versus KO), 0.0020 (Parental versus WT), <0.0001 (Parental versus +KK), <0.0001 (+WT versus KO), and 0.2073 (+WT versus +KK). Scale bars, 25 μm (micrographs) and 5 μm (magnified images). Molecular masses are given in kilodaltons. Bars, error bars, and symbols represent the mean, SEM, and individual data points, respectively. $^{*}P < 0.05$, $^{**}P < 0.01$, $^{***}P < 0.001$, $^{****}P < 0.0001$, ns = not significant. The data underlying the graphs shown in the figure can be found in S1 Data. ESCPE-1, endosomal SNX-BAR sorting complex for promoting exit 1; KO, knockout; SNX1, sorting nexin-1; SNX6, sorting nexin-6; SNX27, sorting nexin-27; WT, wild-type.

https://doi.org/10.1371/journal.pbio.3001601.g006

The association between SNX27 and ESCPE-1 depends on the presence of binding motifs in SNX1 and SNX2 and the FERM domain of SNX27. SNX1 is present across eukaryotes; a gene duplication giving rise to SNX1 and SNX2 from a single ancestral protein occurred in the common ancestor of vertebrates (Figs 7B and S4C). Several motifs required in the FERM domain of *H. sapiens* SNX27 for binding to ESCPE-1 appear to have evolved in the common ancestor of metazoans or early during their radiation (Fig 7B); many of the key residues (R437, R498, and K501) were in place in the last metazoan common ancestor or prior to the divergence of cnidarians and bilaterians (K495 and K496). For SNX1, the first aDLF motif was likely already present in the last metazoan common ancestor. It is present in sequences from bilaterians and Porifera (sponges) but is absent in cnidarians, placazoans, and ctenophorans, which might represent secondary losses of the motif. As for the second aDLF motif, this is present in all vertebrates. This analysis therefore suggests that the SNX27:ESCPE-1 interaction evolved after the SNX27–Retromer link during early metazoan evolution.

## Discussion

Here, in combining biochemical, structural, and cellular analyses, we have established that aDLF motifs in the redundant SNX1 and SNX2 subunits of ESCPE-1 directly associate with the FERM domain of SNX27 within the SNX27–Retromer assembly. Studies of endosomal cargo sorting show that this association is necessary to promote the ESCPE-1-dependent tubulovesicular cell surface recycling of internalized transmembrane proteins. Our data suggest that ESCPE-1 mediated recycling occurs subsequently or in conjunction with SNX27–Retromer-dependent retrieval from lysosomal degradation. Building on previous studies [12–14], these data collectively identify the SNX27:Retromer:ESCPE-1 assembly as a dynamic endosomal coat complex that couples sequence-dependent cargo recognition with membrane remodeling to facilitate the formation of cargo-enriched transport carriers for cargo recycling. In addition, we have begun to describe the functional diversification of Retromer as it has evolved from its tight association with the SNX-BAR homologues Vps5 and Vps17, as originally identified in yeast [50], to a more transient engagement of ESCPE-1 in metazoans and their relatives mediated at least in part through the SNX27 cargo adaptor.

At present, we propose the following model to describe the functional connectivity of the SNX27:Retromer:ESCPE-1 coat complex within the context of cargo retrieval and recycling. Newly endocytosed cargo containing a functional SNX27 PDZbm are recognized by SNX27, associated with the PI(3)P-enriched early endosome, and these interactions together can stabilize the endosomal residency of SNX27 [45]. As the endosome matures, SNX27 binds to

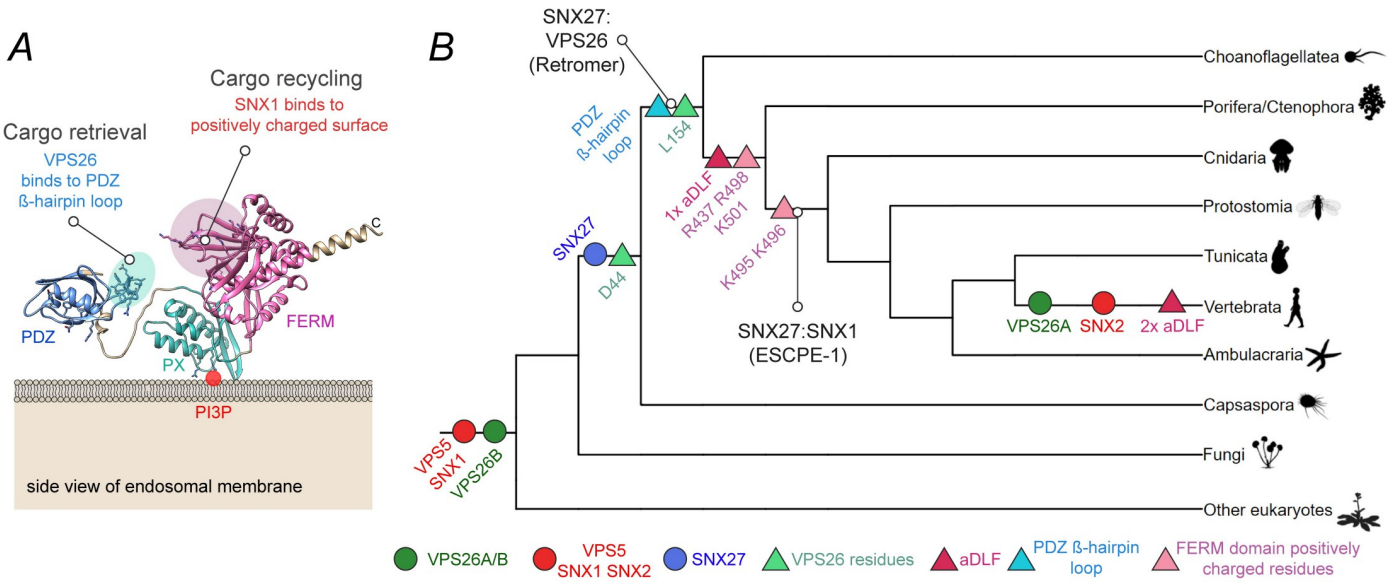


**Fig 7. Molecular evolution of the SNX27–Retromer and SNX27-ESCPE-1 interactions. (A)** Alphafold2 structural prediction for FL human SNX27 [44]. The residues of the exposed ß-hairpin loop in the SNX27 PDZ domain (67 to 79) that account for the interaction with Retromer are highlighted in cyan. Those residues of the FERM domain that account for the interaction with ESCPE-1 (positively charged surface) are highlighted in pink. Our data support a model where the interaction between SNX27 and Retromer is required for the retrieval of PDZ cargos away from the degradative fate. Subsequently, the interaction between SNX27 and ESCPE-1 is required for the export and endosome-to-plasma membrane recycling of PDZ cargos. **(B)** A cartoon representation incorporating the results of multiple phylogenetic analyses, including VPS5/SNX1/SNX2, SNX27, and VPS26A/VPS26B (see S4A–S4C Fig for detailed phylogenies). The gene families that contain VPS5/SNX1/SNX2 and VPS26A/VPS26B are present across eukaryotes: SNX1 and SNX2 and VPS26A and VPS26B, arose by gene duplication in the common ancestor of vertebrates. SNX27 is found in metazoans, choanoflagellates and the filasterean *Capsaspora*, but not in more distantly related opisthokonts such as Ichthyosporea or fungi; it is therefore likely arose in the filazoan common ancestor. The residue D44 (VPS26B, *Homo sapiens*) in VPS26 is found across Filazoa, laying the foundations for the binding interaction between VPS26 and SNX27. L154 (VPS26B, *H. sapiens*) likely arose in the ancestral choanozoan along with the PDZ loop and key interacting residues (67 to 97 L67, L74, SNX27, *H. sapiens*), suggesting that the SNX27–Retromer interaction was already present in the common ancestor of metazoans and choanoflagellates. Key residues of the FERM domain: R437, R498, and K501 (SNX27, *H. sapiens*) are recognizable in the ancestral metazoan. The first aDLF motif (SNX1) was acquired in the common ancestor of cnidarians and bilaterians, along with the residues K495 and K496, which make up part of the FERM domain in SNX27, potentially suggesting that SNX27:ESCPE-1 binding has evolved by this time, if not earlier during metazoan evolution. Interestingly, the first aDLF motif does not appear to be present in the placazoan or ctenophoran sequences, (although the R437, R498, and K501 residues are present), which might reflect secondary loss of the motif in these groups. The second aDLF motif is only present in vertebrates.

https://doi.org/10.1371/journal.pbio.3001601.g007

Retromer through direct association of VPS26A (or VPS26B) to the SNX27 PDZ domain. These interactions are mutually stabilizing, thereby locking down cargo association [14,29]: This assembly is essential for cargo retrieval from the lysosomal degradative fate [13]. Retromer dimerization and the formation of Retromer arches [9,10,33] may aid SNX27 and cargo clustering, thereby forming the retrieval subdomain and initiating weak membrane curvature [51]. These events are supported through the Retromer-mediated recruitment of the WASH complex and the localized production of branched filamentous actin [34,35]. An additional accessory protein, ANKRD50, may serve to stabilize the formation of the SNX27:Retromer:WASH assembly [52]. To this emerging "bud," ESCPE-1 is recruited through recognition of 3-phosphoinositides and membrane curvature [41,53,54] and the direct binding to SNX27 described in the present study. The timed increase in ESCPE-1 residency and localized concentration provides the handover mechanism to ensure that the captured and enriched cargo enter the forming tubular profile and the ensuing transport carrier. Continued localized WASH-mediated actin polymerization and the recruitment of motor proteins facilitates tubule maturation and fission [55–57] (Fig 8). Additional cargo entry may be achieved through direct recognition by ESCPE-1 and yet to be described mechanisms [18,19]. As with the assembly of other coat complexes [58], association of the SNX27:Retromer:ESCPE-1 coat is driven by avidity through a series of low affinity interactions that evoke the consideration of checkpoints for

monitoring the fidelity of pathway progression. It is important to state that this model is certainly an oversimplification and many key questions remain unanswered. Not least whether such a coat complex can be visualized through membrane associated cryo-electron tomography of reconstituted SNX27:Retromer:ESCPE-1 perhaps in the presence of ANKRD50.

The importance of the amino-terminal extension of SNX1 and SNX2 has not previously been considered. While we and others [59–60] have independently established that they constitute primary sites of interaction with SNX27, it is tempting to speculate that they could orchestrate a broader set of protein–protein interactions. Interestingly, these unstructured amino termini may extend to over 30 nm in length and could allow the ESCPE-1 oligomeric assemblies to capture peripheral factors for the fine-tuned regulation of tubular maturation and scission. This would resemble the organization of the endocytic clathrin coat where several accessory proteins protrude from the core clathrin lattice into the cytoplasm to enable a regulated function of the endocytic coat during endocytic vesicle formation [61].

Other than mediating the recruitment of accessory proteins, there is some evidence that these amino-terminal extensions could play a role in the assembly and membrane targeting of SNX-BAR dimers. In fact, besides SNX1 and SNX2, SNX4, SNX7, SNX8, and SNX30, all possess unstructured amino-terminal extensions of different length and of unknown function. The low-complexity region of the SNX8 homologue Mvp1 appears to stabilize soluble Mvp1 in a cytosolic tetrameric form where the PX and BAR domains are masked and unable to target membranes [62]. The release of the amino terminus liberates functional dimers of Mvp1 facilitating their membrane association and function [62]. It will be interesting to explore whether a similar mechanism also regulates ESCPE-1 targeting to the endosomal network in mammalian cells during endosomal recycling.

An important aspect of cargo sorting by SNX27 is regulation by posttranslational modification. Phosphorylation of residues within the core carboxyl-terminal PDZbm negatively impairs SNX27 association, but phosphorylation of residues preceding the minimal PDZbm can dramatically enhance affinity for the SNX27 PDZ domain [29]. A well-characterized example of cargo tail phosphorylation modulating SNX27 affinity and subsequent endosomal sorting is the β2AR [29,63]. Furthermore, phosphorylation of SNX27 at Ser-51 alters the conformation of its PDZbm-binding pocket decreasing the affinity for cargo proteins, thereby inhibiting endosomal sorting [64] and Ser-302 and Ser-304 phosphorylation in VPS26B can modulate SNX27 association [65]. Similarly, ESCPE-1 function can be regulated by phosphorylation; in this case, Ser-226 of SNX5 undergoes phosphorylation, which decreases dimerization with SNX1 and SNX2 and reduces endosomal recycling [66]. Therefore, a fascinating question regards whether the SNX27:ESCPE-1 interaction may be orchestrated by posttranslational modification. We have here shown that a series of acidic residues upstream of the DLF motif in the SNX1 and SNX2 amino termini contribute to the binding to SNX27 (Fig 3F). Interestingly, several phosphorylation sites in the aDLF sequences of SNX1 have been annotated, including Ser-39, Ser-41, and Ser-72, as well as Thr-72 [67–69]. It is tempting to speculate that multiple phosphorylations of the ESCPE-1 amino termini may regulate its association with SNX27–Retromer and, in turn, dictate the timing and kinetics of the endosomal recycling route.

Finally, a fascinating question relates to the molecular evolution of Retromer [70]. In yeast, Retromer can form a stable pentameric assembly of 2 subcomplexes, the so called "cargo-selective" Vps26:Vps35p:Vps29p heterotrimer and the membrane remodeling Vps5p and Vps17p heterodimer [50], the latter being considered analogous to ESCPE-1. Two functional processes, sequence-dependent cargo recognition and the biogenesis of tubulovesicular transport carriers, are therefore brought together in a single pentameric assembly [71]. In metazoans, the VPS26:VPS35:VPS29 Retromer and ESCPE-1 appear to no longer form a stable pentameric assembly [72]; rather, they have diverged into 2 separate

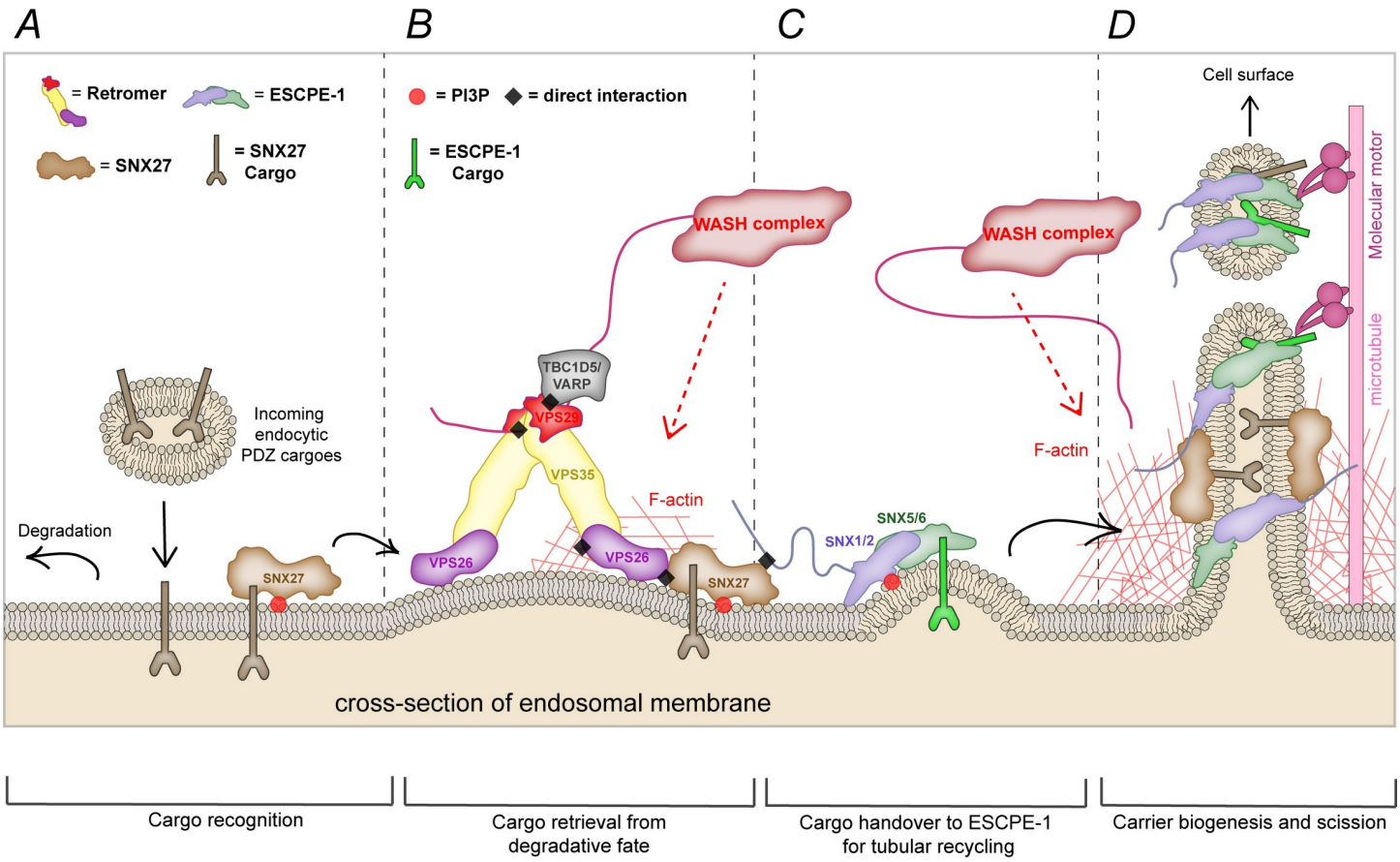


**Fig 8. A 2-step model for the endosomal sorting of SNX27 cargos. (A)** Schematics of the endosomal sorting of PDZ cargos. Cargos possessing a PDZbm that enter the endosomal system are recognized by SNX27 via its PDZ domain. **(B)** SNX27 binding to Retromer aids the retrieval of cargos from the lysosomal degradative path. **(C)** Once cargos have been retrieved, the SNX27 FERM engages the amino terminus of SNX1 and SNX2 mediating the inclusion of SNX27 cargos into ESCPE-1 tubulovesicular carriers. **(D)** This mechanism results in SNX27 cargos entering carriers that exit endosomes and are transported, directly and/or indirectly, to the cell surface. ESCPE-1, endosomal SNX-BAR sorting complex for promoting exit 1; PDZbm, PDZ-binding motif; SNX1, sorting nexin-1; SNX2, sorting nexin-2; SNX27, sorting nexin-27; WASH, Wiskott–Aldrich syndrome protein and SCAR homologue.

https://doi.org/10.1371/journal.pbio.3001601.g008

complexes and in so doing have expanded their functional roles [18,19,49,72,73]. Our phylogenetic analysis suggests that the SNX27:Retromer:ESCPE-1 assembly observed in metazoans evolved in a stepwise manner, with the SNX27–Retromer interaction evolving prior to the origin of metazoans, in the common ancestor of metazoans and choanoflagellates—the group of unicellular and colonical flagellates that are the closest living relatives of animals. The SNX27:ESCPE-1 interaction evolved later, during early metazoan evolution and likely prior to the divergence of cnidarians and bilaterians. Thus, within the SNX27:Retromer:ESCPE-1 pathway, the retrieval of cargo from the degradative fate appears to have evolved prior to the direct coupling to ESCPE-1 for promotion of tubulovesicular-based recycling to the cell surface. The divergence of the ancestral pentameric Retromer coat complex therefore appears to have occurred to accommodate the expanding complexity of the endomembrane system in metazoans [74]. The ability of metazoan Retromer to associate with SNX27 and the ability of ESCPE-1 to directly bind cargo through a helix–loop–helix region [18,19], features not observed in yeast, have greatly expanded the capacity for sequence-dependent endosomal retrieval and recycling in metazoans. Indeed, it is tempting to speculate that the increased plasticity of the SNX27:Retromer:ESCPE-1 axis, and the

existence of additional Retromer-independent pathways [1], has allowed the metazoan endosomal network to accommodate the evolving diversity and number of cargos undergoing sequence-dependent sorting, leading to an expansion in the number of recycling itineraries that cargos can engage to interface with distinct membrane compartments. Dissecting how these sorting complexes and pathways are integrated and regulated, for example, by posttranslational modifications, to shape sequence-dependent cargo sorting within the metazoan endosomal network will be a major challenge moving forward.

Overall, in defining the mechanistic basis of SNX27–Retromer association with ESCPE-1, we have provided new functional insight into the endosomal sorting of hundreds of internalized PDZbm-containing receptors, channels, transporter, enzymes, and adhesion molecules for repopulation of the cell surface [13]. This increased molecular understanding provides new insight into the role of sequence-dependent endosome sorting in cellular processes ranging from the establishment of polarity and the uptake of nutrients through to synaptic function and cancer cell metastasis in both health and disease [40].

## Material and methods

### Antibodies

Antibodies used in this study were mouse monoclonal antibodies GFP (clones 7.1 and 13.1; 11814460001; Roche, Germany) (1:2,000 for WB), LAMP1 (clone H4A3, AB2296838; DSHB, USA) (IF 1:200), SNX1 (clone 51/SNX1; 611482; BD, USA) (1:1,000 for WB, 1:200 for IF), SNX2 (clone 13/SNX2; 5345661; BD) (1:1,000 for WB, 1:200 for IF), SNX6 (clone d-5, 365965; Santa Cruz Biotechnology, USA) (1:1,000 for WB, 1:200 for IF), SNX27 (ab77799, Abcam, UK) (1:1,000 for WB, 1:200 for IF), β-actin (A1978; Sigma-Aldrich, USA) (1:2,000 for WB), ITGA5 (610633, BD) (1:1,000 for WB), VPS29 (clone d-1, 398874; Santa Cruz Biotechnology) (1:200 for WB); rabbit monoclonal antibodies: EEA1 (C45B10; Cell Signaling Technology, USA) (IF 1:200), VPS35 (EPR11501(B); 157220; Abcam) (1:1,000 for WB), GLUT1 (ab115730, Abcam) (1:1,000 for WB, 1:200 for IF); rabbit polyclonal antibodies: GFP (GTX20290; GeneTex, USA) (WB 1:2,000), VPS26A (23892; Abcam) (1:1,000 for WB), VPS35 (97545; Abcam) (1:1,000 for WB, 1:200 for IF), VPS29 (98929; Abcam) (1:100 for WB); and goat polyclonal antibodies to VPS35 (10099; Abcam) (1:200 for IF).

### Cell culture and transfection

HeLa and HEK-293T cell lines were sourced from ATCC. Authentication was from the ATCC. Cells were grown in DMEM (Sigma-Aldrich) supplemented with 10% (v/v) FCS (Sigma-Aldrich) and penicillin/streptomycin (Gibco, USA) and grown under standard conditions. FuGENE HD (Promega, USA) was used for transient transfection of DNA according to the manufacturer's instructions. Cycloheximide was used to prevent up-regulation of protein synthesis. In this case, cycloheximide (C7698; Sigma-Aldrich) at 10 μg/ml was added to the cells 48 hours after FuGENE transfection for the indicated time points. For the generation of CRISPR-Cas9 SNX27 knockout HeLa cells, HeLa cells were transfected with pX330 plasmid coding for the gRNA against the gene of interest together with a puromycin resistance–expressing plasmid. Cells were then subjected to puromycin selection for 24 hours. The pooled population of cells was subjected to lysis and western blotting to confirm the knockout. The VPS35 knockout clonal cell line used in this study was characterized previously [73]. For GFP-based immunoprecipitations, HEK293T cells were transfected with GFP constructs using polyethylenimine (Sigma-Aldrich) and expression was allowed for 48 hours.

## Immunoprecipitation and quantitative western blot analysis

For western blotting, cells were lysed in PBS with 1% (v/v) Triton X-100 and protease inhibitor cocktail. The protein concentration was determined with a BCA assay kit (Thermo Fisher Scientific, USA), and equal amounts were resolved on NuPAGE 4% to 12% precast gels (Invitrogen, USA). Blotting was performed onto polyvinylidene fluoride membranes (Immobilon-FL; EMD Millipore, USA) followed by detection using the Odyssey infrared scanning system (LI-COR Biosciences, USA). For GFP-based immunoprecipitations, HEK-293T cells were lysed 48 hours after transfection in immunoprecipitation buffer (50 mM Tris-HCl, 0.5% (v/v) NP-40, and Roche protease inhibitor cocktail) and subjected to GFP trap (ChromoTek, Germany). Immunoblotting was performed using standard procedures. Detection was performed on an Odyssey infrared scanning system (LI-COR Biosciences) using fluorescently labeled secondary antibodies. In using the Odyssey, we routinely performed western blot analysis where a single blot is simultaneously probed with antibodies against 2 proteins of interest (distinct antibody species) followed by visualization with the corresponding secondary antibodies conjugated to distinct spectral dyes.

## Biotinylation of cell surface proteins

For surface biotinylation experiments, fresh Sulfo-NHS-SS Biotin (Thermo Fisher Scientific, #21217) was dissolved in ice-cold PBS at pH 7.8 at a final concentration of 0.2 mg/ml. Cells were washed twice in ice-cold PBS and placed on ice to slow down the endocytic pathway. Next, cells were incubated with the biotinylation reagent for 30 minutes at 4˚C followed by incubation in TBS for 10 minutes to quench the unbound biotin. The cells were then lysed in lysis buffer and subjected to Streptavidin beads-based affinity isolation (GE Healthcare, USA).

## Immunofluorescence staining

Cells were fixed in 4% (v/v) PFA for 20 minutes and washed 3 times in PBS and permeabilized with 0.1% (v/v) Triton X-100. For LAMP1 staining, cells were instead permeabilized by submersion in liquid nitrogen for 20 seconds. Fixed cells were blocked in 1% (w/v) BSA and incubated in primary antibody and respective secondary antibody (Alexa Fluor; Thermo Fisher Scientific) in 1% (w/v) BSA.

## Image acquisition and image analysis

Microscopy images were collected with a confocal laser-scanning microscope (SP5 AOBS; Leica Microsystems, Germany) attached to an inverted epifluorescence microscope (DMI6000; Thermo Fisher Scientific). A 63× 1.4 NA oil immersion objective (Plan Apochromat BL; Leica Biosystems, Germany) and the standard SP5 system acquisition software and detector were used. Images were captured at room temperature as z stacks with photomultiplier tube detectors with a photocathode made of gallium-arsenide-phosphide (Leica Microsystems) for collecting light emission. Images were captured using Application Suite AF software (version 2.7.3.9723; Leica Microsystems) and then analyzed with the Volocity 6.3 software (PerkinElmer, USA).

## Statistics and reproducibility

All quantified western blot are the mean of at least 3 independent experiments. Statistical analyses were performed using Prism 7 (GraphPad Software, USA). Graphs represent means and SEM For all statistical tests, $P < 0.05$ was considered significant and is indicated by asterisks.

## Molecular biology and cloning for recombinant protein production

For bacterial expression, full-length mouse SNX1 with an amino-terminal His-tag ($mSNX1_{FL}$ hereafter) was cloned into the pMW172Kan vector [75], and the truncated mSNX1 construct containing residues 1 to 139 was cloned into pGEX4T-2 vector for expression as a thrombin-cleavable amino-terminal GST fusion protein. DNA encoding full-length mouse SNX27 ($mSNX27_{FL}$ hereafter) was inserted into the pMCSG7 vector [76] by the ligation-independent cloning (LIC) approach. Human SNX27 constructs, $hSNX27_{FL}$, $hSNX27_{FERM}$, and $hSNX27_{FL}$ single-site mutants R437D, K495D, K496D, R498D, and K501D were cloned into the pET-28a vector by GenScript and codon optimized for bacterial protein expression. An additional TEV cleavage site was inserted between the amino-terminal His-tag and hSNX27 coding sequences.

## Protein expression and purification

The DNA constructs of mSNX27 and mSNX1 were expressed using *Escherichia coli* BL21 CodonPlus (DE3) competent cells, while the hSNX27 constructs were expressed using *E. coli* BL21 (DE3) competent cells. The cells were grown in Ultra Yield flasks at 37˚C, 180 rpm until the cell density reached $OD_{600}$ approximately 0.8. Protein expression was then induced with 1 mM IPTG and cells incubated for 16 to 18 hours at 18˚C. For SNX27, 0.5 mM IPTG was added for induction to get optimal protein expression yield. To collect cell pellets, the cells were harvested by 10-minute centrifugation (JLA 8.1 rotor) at 6,000 rpm, 4˚C.

For SNX1 purification, the cell pellet was resuspended in lysis buffer containing 50 mM HEPES pH 7.5, 200 mM NaCl, 5% glycerol, 1 mM β-mercaptoethanol (β-ME), 1 mM benzamidine, and 10 μg/mL DNase I dissolved in PBS containing 10% glycerol. For SNX27 proteins, the cell pellet was resuspended in lysis buffer containing 20 mM Tris-HCl pH 8.0, 500 mM NaCl, 5% glycerol, 1 mM β-ME, 1% Triton X-100, 1 mM benzamidine, and 10 μg/mL DNase I dissolved in PBS containing 10% glycerol. Cells were lysed by high-pressure homogenization (35 Kpsi). The homogenate was centrifuged for 30 minutes at 4˚C using a JA 25.50 rotor with 19,000 rpm. The supernatant of His-tagged protein homogenates were loaded onto preequilibrated TALON metal affinity resin (Clontech, USA) or Ni-nitrilotriacetic acid (NTA) resin, while the supernatant of GST-fusion protein homogenates were loaded onto preequilibrated glutathione Sepharose beads (GE Healthcare) and incubated on an orbital rotator for an hour in cold room.

Affinity matrices with bound fusion proteins were loaded into empty glass chromatography columns (Bio-Rad, USA) washed with 100 ml of washing buffer containing either 50 mM HEPES pH 7.5, 200 mM NaCl, 5% glycerol, 1 mM β-ME or 20 mM Tris-HCl pH 8.0, 200 mM NaCl, 5% glycerol, 1 mM β-ME. For His-tagged protein purification, 10 mM and 300 mM imidazole was added to wash and elution buffers, respectively. To collect the GST-tagged mSNX1 constructs, 50 mM reduced glutathione in elution buffer was applied for elution. cOmplete EDTA-free protease inhibitor tablets were added to the eluted SNX1 samples to reduce proteolytic degradation of their disordered amino-terminal region.

The fractions containing eluted proteins were concentrated to approximately 5 ml by Amicon cc ultrafiltration devices (10 kDa or 30 kDa molecular mass cutoff) (Millipore) and centrifuged in a bench centrifuge for 10 minutes at maximum speed to remove any precipitated material before being subjected to size-exclusion chromatography (SEC). For SEC, the HiLoad 16/600 Superdex 200 (GE Healthcare) column was used with proteins eluted in SEC buffer containing 50 mM HEPES pH 7.5, 200 mM NaCl, 5% glycerol, 1 mM β-ME or 20 mM Tris-HCl pH 8.0, 100 mM NaCl, 5% glycerol, and 1 mM β-ME. To check the purify and integrity of the purified fractions, sodium dodecyl sulfate-polyacrylamide gel electrophoresis (SDS-PAGE) was applied using Bolt 12% Bis-Tris gel with 1x MES running buffer at 190V for 25 minutes.

After the SDS-PAGE, gels were stained with Coomassie Brilliant Blue R250 solution for visualization. For $hSNX27_{FERM}$, an additional anion exchange chromatography (IEX) was applied using the Mono Q anion exchange chromatography column preequilibrated with IEX buffer A: 20 mM Tris-HCl pH 8.0, 100 mM NaCl, 5% glycerol, 1 mM β-ME. A linear salt gradient from 0% to 40% IEX buffer B (20 mM Tris-HCl pH 8.0, 500 mM NaCl, 5% glycerol, 1 mM β-ME) was conducted. Proteins usually eluted in buffer containing 200 mM NaCl, and fractions collected were analyzed by SDS-PAGE.

## Isothermal titration calorimetry

Human SNX1 and SNX2 peptide sequences were synthesized by Genscript (USA). To obtain the peptide stock solutions at neutral pH, 100 mM Tris-HCl, pH 10.6 was used to dissolve the peptide to a final concentration of 8 mM. The peptides were $SNX1_{35\text{-}51}$ EAGDSDTEGEDIFTGAA, $SNX_{135\text{-}51(D45K)}$ EAGDSDTEGEKIFTGAA, $SNX1_{75\text{-}92}$ NGIHEEQDQEPQDLFADA, $SNX2_{16\text{-}33}$ TDFEDLEDGEDLFTSTVS, $SNX2_{16\text{-}33(DLF/SSS)}$ TDFEDLEDGESSSTSTVS, and $SNX2_{62\text{-}82}$ TEVVLDDDREDLFAEATEEVS.

All microcalorimetry experiments were conducted at 25˚C using a PEAQ ITC (Malvern, UK) in 50 mM HEPES (pH 7.5), 200 mM NaCl, 5% glycerol, and 1 mM β-ME (ITC buffer). All proteins were purified by SEC using the same buffer prior to ITC experiments to avoid buffer mismatches. To measure binding of SNX27 to SNX1 proteins, 800 μM of $hSNX27_{FERM}$ was titrated into 20 μM of GST-$mSNX1_{1\text{-}139}$ or His-$SNX1_{FL}$. For the binding of SNX1 and SNX2 peptides to SNX27, peptides were diluted 10-fold to 800 μM in ITC buffer peptides and titrated into 20 μM $SNX27_{FL}$ proteins containing the same 1:10 ratio of peptide buffer (100 mM Tris-HCl, pH 10.6). The competitive ITC experiments were carried out by titrating 800 μM $SNX1_{75\text{-}92}$ peptides into 20 μM proteins with 2-fold molar excess $SNX2_{16\text{-}33}$ peptide preincubated with SNX27 on ice for an hour. For ITC experiment using $SNX1_{75\text{-}92}$ against hSNX27 wild-type and single-site mutants, 600 μM $SNX1_{75\text{-}92}$ peptide was titrated into 20 μM hSNX27 proteins.

The ITC experiments were conducted with 1 injection of 0.4 μL followed by a series of 12 injections of 3.2 μL each with 180-second intervals and a stirring speed of 850 rpm. The heat exchange of interactions was obtained through integrating the observed peaks and background correction by subtracting the heats of dilution. Data were analyzed with Malvern software package by fitting and normalized data to a single-site binding model, yielding the thermodynamic parameters $K_d$, $\Delta H$, $\Delta G$, and $-T\Delta S$ for all binding experiments. The stoichiometry was refined initially, and if the value was close to 1, then N was set to exactly 1.0 for calculation. All experiments were performed at least twice to guarantee reproducibility of the data.

## AlphaFold predictions of peptide binding to SNX27

To generate predicted models of SNX1 and SNX2 amino-terminal peptides associating with the SNX27 FERM domain, we used the AlphaFold2 neural network [47] implemented within the freely accessible ColabFold pipeline [48]. For each peptide-modeling experiment, the sequence of the human SNX27a FERM domain (residues 269 to 531; Q96L92) was modeled with the 4 separate amino-terminal aDLF sequences from SNX1 and SNX2. The specific peptides we modeled were residues 33 to 56 and 75 to 98 from human SNX1 (Q13596) and residues 14 to 37 and 60 to 83 from human SNX2 (O60749). ColabFold was executed using default settings where multiple sequence alignments were generated with MMseqs2 [77], and structural relaxation of final peptide geometry was performed with Amber [78] to generate 3 models per peptide. Sequence conservation was mapped onto the modeled SNX27 FERM domain structure with Consurf [79]. Structural alignments and images were generated with Pymol (Schrodinger, USA).

## Phylogenetic analyses

Homologous proteins were identified using NCBI protein–protein BLAST (with default parameters) against all non-redundant GenBank CDS Translations+PDB+SwissProt+PIR+PRF excluding environmental samples from WGS projects for a wider range of species (unaligned sequence data with accession numbers available in S4 Fig). For the ctenophore data, we used the BLAST (with default parameters) from the Mnemiopsis Genome Project Portal (MGP) portal [80–82]. Sequences were aligned using MAFFT v7.480 [83], L-INS-I mode, and then used to infer initial exploratory trees to identify specific duplications (using IQtree 2.1.4 [84] with the LG+F+G model and 1,000 ultrafast bootstraps). After orthologues of each copy of the gene were identified in a range of taxa, we then performed iterative tree inferences to confirm paralogues and to identify species-specific duplication events. Subsequent maximum likelihood phylogenetic analyses were performed using IQtree 2.1.4 with the best fitting model selected using the Bayesian information criterion (BIC), including models which account for site-rate heterogeneity (LG+C10 . . .C60) [85], empirical amino acid frequencies (+F), and accounting for across-site rate variation using either a Gamma distribution (+G) [86] or the free rates model (+R) [87,88] with 10,000 ultrafast bootstrap replicates. The best fitting model according to BIC was LG+C30+F+G for the final SNX1 and SNX2 tree (see S4 Fig) and LG+C20+F+G for SNX27 and VPS26 (alignments and maximum likelihood trees in S4 Fig).

## Supporting information

**S1 Fig. Western blot showing the levels of GLUT1 in parental HeLa, VPS35 KO, and SNX27KO not transfected or transiently transfected with GFP-SNX27 WT, GFP-SNX27 Δ67–77, and GFP-SNX27 ΔFERM.** The blot is representative of 3 independent assays. Molecular masses are given in kilodaltons. Bars, error bars, and symbols represent the mean, SEM, and individual data points, respectively. $^{*}P < 0.05$, $^{**}P < 0.01$, $^{***}P < 0.001$, $^{****}P < 0.0001$, ns = not significant. The data underlying the graphs shown in the figure can be found in S1 Data. KO, knockout; SNX27, sorting nexin-27; WT, wild-type.
(TIF)

**S2 Fig.** **(A)** Co-immunoprecipitation of GFP-tagged extended amino-terminal regions (NT) of SNX1 and SNX2 alongside the GFP-tagged short amino-terminal regions of SNX5 and SNX6 expressed in HEK293T cells. The cell lysates were subjected to GFP trap–based immunoprecipitation and the immunoprecipitates were blotted for SNX27 and GFP. The blot is representative of 3 independent GFP traps. **(B)** Co-immunoprecipitation of GFP-tagged SNX2 WT or SNX2 KK (D27K, D72K) expressed in HEK293T cells. The cell lysates were subjected to GFP trap–based immunoprecipitation and the immunoprecipitates were blotted for SNX27, SNX6, and GFP. The blot is representative of 4 independent GFP traps. **(C)** Competitive ITC assay of $SNX2_{16\text{-}33}$ and $mSNX27_{FL}$ preincubated with 2-fold molar excess of $SNX1_{75\text{-}92}$ peptide showing that binding is blocked by the competing $SNX1_{75\text{-}92}$ peptide. Molecular masses are given in kilodaltons. Bars, error bars, and symbols represent the mean, SEM, and individual data points, respectively. $^{*}P < 0.05$, $^{**}P < 0.01$, $^{***}P < 0.001$, $^{****}P < 0.0001$, ns = not significant. The data underlying the graphs shown in the figure can be found in S1 Data. SNX1, sorting nexin-1; SNX5, sorting nexin-5; SNX6, sorting nexin-6; SNX27, sorting nexin-27; WT, wild-type.
(TIF)

**S3 Fig.** **(A)** SNX27 surface colored according to sequence conservation. The peptides are predicted to bind to a highly conserved pocket in SNX27. **(B, C)** As described in methods, 12 models of SNX27 were generated in total, consisting of 3 models each of SNX27 in association

with the 4 aDLF sequences from human SNX1 and SNX2. B shows the overlay of all 12 models in Cα trace representation colored by the pLDDT score. The pLDDT is a per-residue confidence score between 0 (lowest confidence) and 100 (highest confidence). The majority of the SNX27 structures show very high pLDDT scores and overlay with very high precision. C shows only the best 8 models where the core aDLF sequences have identical binding conformations. aDLF, acidic-Asp-Leu-Phe; pLDDT, predicted Local Distance Difference Test; SNX1, sorting nexin-1; SNX2, sorting nexin-2; SNX27, sorting nexin-27.
(TIF)

**S4 Fig. Maximum likelihood phylogenies of (A) SNX27, (B) VPS26A/B and (C) VPS5/SNX1/SNX2. (A)** SNX27 (green) with SNX17 (red) used as an outgroup with representatives across Filozoa. Amino acids aligned with *Homo sapiens* in positions 437, 495, 496, 498, and 501 are written next to the species name. **(B)** VPS26A, VPS26B, and VPS26C, with VPS26C in red and VPS26B in green; the duplication event occurring in the ancestral vertebrate is in blue. Interestingly, we also find another independent duplication of VPS26B in plants evidenced by *Arabidopsis thaliana* and *Quercus suber* in this tree. **(C)** The SNX1 sequences across choanozoans, with the duplication in vertebrates in blue. The number of aDLF motifs in the amino terminus is written next to the species name. Phylogenies were inferred under the best-fit model as determined by BIC. Branch support values are percentages based on 10,000 ultrafast bootstraps. aDLF, acidic-Asp-Leu-Phe; BIC, Bayesian information criterion; SNX1, sorting nexin-1; SNX27, sorting nexin-27.
(TIF)

**S1 Table. Summary of ITC binding parameters.** ITC, isothermal titration calorimetry.
(PDF)

**S1 Raw Images. Unprocessed images for blots shown in the paper.**
(PDF)

**S1 Data. Numerical data for Figs 1B, 1C, 2C, 3A, 3C, 3F, 4D, 4G, 5A, 5B, 5C, 5D, 5E, 6A, 6B, 6C, 6D and 6E and S1A and S2B.**
(XLSX)

## Acknowledgments

We thank the Wolfson Bioimaging Facility at the University of Bristol for their support.

## Author Contributions

**Conceptualization:** Boris Simonetti, Brett M. Collins, Peter J. Cullen.

**Data curation:** Boris Simonetti, Qian Guo, Manuel Giménez-Andrés, Kai-En Chen, Edmund R. R. Moody, Mintu Chandra.

**Formal analysis:** Boris Simonetti, Qian Guo, Manuel Giménez-Andrés, Kai-En Chen, Edmund R. R. Moody, Mintu Chandra.

**Funding acquisition:** Tom A. Williams, Brett M. Collins, Peter J. Cullen.

**Investigation:** Boris Simonetti, Qian Guo, Manuel Giménez-Andrés, Kai-En Chen, Edmund R. R. Moody, Ashley J. Evans, Mintu Chandra, Chris M. Danson, Tom A. Williams, Brett M. Collins, Peter J. Cullen.

**Methodology:** Edmund R. R. Moody, Tom A. Williams.

**Project administration:** Boris Simonetti, Tom A. Williams, Brett M. Collins, Peter J. Cullen.

**Resources:** Boris Simonetti, Tom A. Williams, Brett M. Collins, Peter J. Cullen.

**Supervision:** Boris Simonetti, Tom A. Williams, Brett M. Collins, Peter J. Cullen.

**Validation:** Boris Simonetti, Qian Guo, Manuel Giménez-Andrés, Kai-En Chen, Edmund R. R. Moody, Ashley J. Evans, Mintu Chandra, Chris M. Danson, Tom A. Williams, Brett M. Collins, Peter J. Cullen.

**Writing – original draft:** Boris Simonetti, Qian Guo, Edmund R. R. Moody, Tom A. Williams, Brett M. Collins, Peter J. Cullen.

**Writing – review & editing:** Boris Simonetti, Qian Guo, Manuel Giménez-Andrés, Kai-En Chen, Edmund R. R. Moody, Ashley J. Evans, Mintu Chandra, Chris M. Danson, Tom A. Williams, Brett M. Collins, Peter J. Cullen.

## References

1. Cullen PJ, Steinberg F. To degrade or not to degrade: mechanisms and significance of endocytic recycling. Nat Rev Mol Cell Biol. 2018; 19:679–96. https://doi.org/10.1038/s41580-018-0053-7 PMID: 30194414
2. Small SA, Petsko GA. Endosomal recycling reconciles the Alzheimer's disease paradox. Sci Transl Med. 2020; 12(eabb1717). https://doi.org/10.1126/scitranslmed.abb1717 PMID: 33268506
3. Maxfield FR, McGraw TE. Endocytic recycling. Nat Rev Mol Cell Biol. 2004; 5:121–32. https://doi.org/10.1038/nrm1315 PMID: 15040445
4. McNally KE, Cullen PJ. Endosomal retrieval of cargo: retromer is not alone. Trends Cell Biol. 2018; 28:807–22. https://doi.org/10.1016/j.tcb.2018.06.005 PMID: 30072228
5. Chen KE, Healy MD, Collins BM. Towards a molecular understanding of endosomal trafficking by Retromer and Retriever. Traffic. 2019; 20:465–78. https://doi.org/10.1111/tra.12649 PMID: 30993794
6. Strochlic TI, Setty TG, Sitaram A, Burd CG. Grd19/Snx3p functions as a cargo-specific adapter for retromer-dependent endocytic recycling. J Cell Biol. 2007; 177:115–25. https://doi.org/10.1083/jcb.200609161 PMID: 17420293
7. Harterink M, Port F, Lorenowicz MJ, McGough IJ, Silhankova M, Betist MC, et al. A SNX3-dependent retromer pathway mediates retrograde transport of the Wnt sorting receptor Wntless and is required for Wnt secretion. Nat Cell Biol. 2011; 13:914–23. https://doi.org/10.1038/ncb2281 PMID: 21725319
8. Lucas M, Gershlick DC, Vidaurrazaga A, Rojas AL, Bonifacino JS, Hierro A. Structural mechanism for cargo recognition by the retromer complex. Cell. 2016; 167:1623–35. https://doi.org/10.1016/j.cell.2016.10.056 PMID: 27889239
9. Kendall AK, Xie B, Xu P, Wang J, Burcham R, Frazier MN, et al. Mammalian retromer is an adaptable scaffold for cargo sorting from endosomes. Structure. 2020; 28:393–405. https://doi.org/10.1016/j.str.2020.01.009 PMID: 32027819
10. Leneva N, Kovtun O, Morado DR, Briggs JAG, Owen DJ. Architecture and mechanism of metazoan retromer:SNX3 tubular coat assembly. Sci Adv. 2021; 7(eabf8598). https://doi.org/10.1126/sciadv.abf8598 PMID: 33762348
11. Lauffer BE, Melero C, Temkin P, Lei C, Hong W, Kortemme T, et al. SNX27 mediates PDZ-directed sorting from endosomes to the plasma membrane. J Cell Biol. 2010; 190:565–74. https://doi.org/10.1083/jcb.201004060 PMID: 20733053
12. Temkin P, Lauffer B, Jager S, Cimermancic P, Krogan NJ, von Zastrow M. SNX27 mediates retromer tubule entry and endosome-to-plasma membrane trafficking of signalling receptors. Nat Cell Biol. 2011; 13:715–21. https://doi.org/10.1038/ncb2252 PMID: 21602791
13. Steinberg F, Gallon M, Winfield M, Thomas EC, Bell AJ, Heesom KJ, et al. A global analysis of SNX27-retromer assembly and cargo specificity reveals a function in glucose and metal ion transport. Nat Cell Biol. 2013; 15:461–71. https://doi.org/10.1038/ncb2721 PMID: 23563491
14. Gallon M, Clairfeuille T, Steinberg F, Mas C, Ghai R, Sessions RB, et al. A unique PDZ domain and arrestin-like fold interaction reveals mechanistic details of endocytic recycling by SNX27-retromer. Proc Natl Acad Sci U S A. 2014; 111:E3604–13. https://doi.org/10.1073/pnas.1410552111 PMID: 25136126
15. McNally KE, Faulkner R, Steinberg F, Gallon M, Ghai R, Pim D, et al. Retriever is a multiprotein complex for retromer-independent endosomal cargo recycling. Nat Cell Biol. 2017; 19:1214–25. https://doi.org/10.1038/ncb3610 PMID: 28892079

16. Phillips-Krawczak CA, Singla A, Starokadomskyy P, Deng Z, Osborne DG, Li H, et al. COMMD1 is linked to the WASH complex and regulates endosomal trafficking of the copper transporter ATP7A. Mol Biol Cell. 2015; 26:91–103. https://doi.org/10.1091/mbc.E14-06-1073 PMID: 25355947

17. Bartuzi P, Billadeau DD, Favier R, Rong S, Dekker D, Fedoseienko FH, et al. CCC- and WASH-mediated endosomal sorting of LDLR is required for normal clearance of circulating LDL. Nat Commun. 2016; 7:10961. https://doi.org/10.1038/ncomms10961 PMID: 26965651

18. Simonetti B, Paul B, Chaudhari K, Weeratunga S, Steinberg F, Gorla M, et al. Molecular identification of a BAR domain-containing coat complex for endosomal recycling of transmembrane proteins. Nat Cell Biol. 2019; 21:1219–33. https://doi.org/10.1038/s41556-019-0393-3 PMID: 31576058

19. Yong X, Zhao L, Deng W, Sun H, Zhou X, Mao L, et al. Mechanism of cargo recognition by retromer-linked SNX-BAR proteins. PLoS Biol. 2020; 18:e3000631. https://doi.org/10.1371/journal.pbio.3000631 PMID: 32150533

20. Gomez TS, Billadeau DD. A FAM21-containing WASH complex regulates retromer-dependent sorting. Dev Cell. 2009; 17:699–711. https://doi.org/10.1016/j.devcel.2009.09.009 PMID: 19922874

21. Derivery E, Sousa C, Gautier JJ, Lombard B, Loew D, Gautreau A. The Arp2/3 activator WASH controls the fission of endosomes through a large multiprotein complex. Dev Cell. 2009; 17:712–23. https://doi.org/10.1016/j.devcel.2009.09.010 PMID: 19922875

22. Kaiji Y, Muraoka S, Hiraoka S, Fujiyama K, Umino A, Nishikawa T. A developmentally regulated and psychostimulant-inducible novel rat gene mrt1 encoding PDZ-PX proteins isolated in the neocortex. Mol Psychiatry. 2003; 8:434–44. https://doi.org/10.1038/sj.mp.4001258 PMID: 12740601

23. Ghai R, Mobli M, Norwood SJ, Bugarcic A, Teasdale RD, King GF, et al. Phox homology band 4.1/ezrin/radixin/moesin-like proteins function as molecular scaffolds that interact with cargo receptors and Ras GTPases. Proc Natl Acad Sci U S A. 2011; 108:7763–8. https://doi.org/10.1073/pnas.1017110108 PMID: 21512128

24. Joubert L, Hanson B, Barthet G, Sebben M, Claeysen S, Hong W, et al. New sorting nexin (SNX27) and NHERF specifically interact with the 5-HT4a receptor splice variant: roles in receptor targeting. J Cell Sci. 2004; 117:5367–79. https://doi.org/10.1242/jcs.01379 PMID: 15466885

25. Lunn M-L, Nassirpour R, Arrabit C, Tan J, McLeod I, Arias CM, et al. A unique sorting nexin regulates trafficking of potassium channels via a PDZ domain interaction. Nat Neurosci. 2007; 10:1249–59. https://doi.org/10.1038/nn1953 PMID: 17828261

26. Balana B, Maslennikov I, Kwiatkowski W, Stern KM, Bahima L, Choe S, et al. Mechanism underlying selective regulation of G protein-gated inwardly rectifying potassium channels by the psychostimulant-sensitive sorting nexin 27. Proc Natl Acad Sci U S A. 2011; 108:5831–6. https://doi.org/10.1073/pnas.1018645108 PMID: 21422294

27. Cai L, Loo LS, Atlashkin V, Hanson BJ, Hong W. Deficiency of sorting nexin 27 (SNX27) leads to growth retardation and elevated levels of N-methyl-D-aspartate receptor 2C (NR2C). Mol Cell Biol. 2011; 31:1734–47. https://doi.org/10.1128/MCB.01044-10 PMID: 21300787

28. Hussain NK, Diering GH, Sole J, Anggono V, Huganir RL. Sorting nexin-27 regulates basal and activity-dependent trafficking of AMPARs. Proc Natl Acad Sci U S A. 2014; 111:11840–5. https://doi.org/10.1073/pnas.1412415111 PMID: 25071192

29. Clairfeuille T, Mas C, Chan AS, Yang Z, Tello-Lafoz M, Chandra M, et al. A molecular code for endosomal recycling of phosphorylated cargos by the SNX27-retromer complex. Nat Struct Mol Biol. 2016; 23:921–32. https://doi.org/10.1038/nsmb.3290 PMID: 27595347

30. Sharma P, Parveen S, Shah LV, Mukherjee M, Kalaidzidis Y, Kozielski AJ, et al. SNX27-retromer assembly recycles MT1-MMP to invadopodia and promotes breast cancer metastasis. J Cell Biol. 2020; 219:e201812098. https://doi.org/10.1083/jcb.201812098 PMID: 31820782

31. McMillan KJ, Banks PJ, Hellel FL, Carmichael RE, Clairfeuille T, Evans AJ, et al. Sorting nexin-27 regulates AMPA receptor trafficking through the synaptic adhesion protein LRFN2. Elife. 2021; 10:e59432. https://doi.org/10.7554/eLife.59432 PMID: 34251337

32. Kerr MC, Bennetts JS, Simpson F, Thomas EC, Flegg C, Gleeson PA, et al. A novel mammalian retromer component, Vps26B. Traffic. 2005; 6:991–1001. https://doi.org/10.1111/j.1600-0854.2005.00328.x PMID: 16190980

33. Kovtun O, Leneva N, Bykov YS, Ariotti N, Teasdale RD, Schaffer M, et al. Structure of the membrane-assembled retromer coat determined by cryo-electron tomography. Nature. 2018; 561:561–4. https://doi.org/10.1038/s41586-018-0526-z PMID: 30224749

34. Harbour ME, Breusegem SY, Seaman MNJ. Recruitment of the endosomal WASH complex is mediated by the extended 'tail' of FAM21 binding to the retromer protein VPS35. Biochem J. 2012; 442:209–20. https://doi.org/10.1042/BJ20111761 PMID: 22070227

35. Jia D, Gomez TS, Billadeau DD, Rosen MK. Multiple repeat elements within the FAM21 tail link the WASH actin regulatory complex to the retromer. Mol Biol Cell. 2012; 23:2352–61. https://doi.org/10.1091/mbc.E11-12-1059 PMID: 22513087

36. Puthenveedu MA, Lauffer B, Temkin P, Vistein R, Carlton P, Thorn K, et al. Sequence-dependent sorting of recycling proteins by actin-stabilized endosomal microdomains. Cell. 2010; 143:761–73. https://doi.org/10.1016/j.cell.2010.10.003 PMID: 21111236

37. Tsvetanova NG, Irannejad R, von Zastrow M. G protein-coupled receptor (GPCR) signaling via heterotrimeric G proteins from endosomes. J Biol Chem. 2015; 290:6689–96. https://doi.org/10.1074/jbc.R114.617951 PMID: 25605726

38. Varandas KC, Irannejad R, von Zastrow M. Retromer endosome exit domains serve multiple trafficking destinations and regulate local G protein activation by GPCRs. Curr Biol. 2016; 26:3129–42. https://doi.org/10.1016/j.cub.2016.09.052 PMID: 27839977

39. Lee S, Chang J, Blackstone C. FAM21 directs SNX27-retromer cargoes to the plasma membrane by preventing transport to the Golgi apparatus. Nat Commun. 2016; 7:10939. https://doi.org/10.1038/ncomms10939 PMID: 26956659

40. Chandra M, Kendall AK, Jackson LP. Toward understanding the molecular role of SNX27/Retromer in human health and disease. Front Cell Dev Biol. 2021; 9:642378. https://doi.org/10.3389/fcell.2021.642378 PMID: 33937239

41. Carlton J, Bujny M, Peter BJ, Oorschot VM, Rutherford A, Mellor H, et al. Sorting nexin-1 mediates tubular endosome-to-TGN transport through coincidence sensing of high-curvature membranes and 3-phosphoinositides. Curr Biol. 2004; 14:1791–800. https://doi.org/10.1016/j.cub.2004.09.077 PMID: 15498486

42. van Weering JRT, Sessions RB, Traer CJ, Kloer DP, Bhatia VK, Stamou D, et al. Molecular basis for SNX-BAR-mediated assembly of distinct endosomal sorting tubules. EMBO J. 2012; 31:4466–80. https://doi.org/10.1038/emboj.2012.283 PMID: 23085988

43. Wassmer T, Attar N, Bujny MV, Oakley J, Traer CJ, Cullen PJ. A loss-of-function screen reveals SNX5 and SNX6 as potential components of the mammalian retromer. J Cell Sci. 2007; 120:45–54. https://doi.org/10.1242/jcs.03302 PMID: 17148574

44. Tunyasuvunakool K, Adler J, Wu Z, Green T, Zielinski M, Zidek A, et al. Highly accurate protein structure prediction for the human proteome. Nature. 2021; 596:590–6. https://doi.org/10.1038/s41586-021-03828-1 PMID: 34293799

45. Ghai R, Bugarcic A, Liu H, Norwood SJ, Skeldal S, Coulson EJ, et al. Structural basis for endosomal trafficking of diverse transmembrane cargos by PX-FERM proteins. Proc Natl Acad Sci U S A. 2013; 110:E643–52. https://doi.org/10.1073/pnas.1216229110 PMID: 23382219

46. Ghai R, Tello-Lafoz M, Norwood SJ, Yang Z, Clairfeuille T, Teasdale RD, et al. Phosphoinositide binding to the SNX27 FERM domain regulates its localization at the immune synapse of activated T-cells. J Cell Sci. 2015; 128:553–65. https://doi.org/10.1242/jcs.158204 PMID: 25472716

47. Jumper J, Evans R, Pritzel A, Green T, Figurnov M, Ronneberger O, et al. Highly accurate protein structure prediction with AlphaFold. Nature. 2021; 15:1–7.

48. Mirdita M, Ovchinnikov S, Steinegger M (2021) ColabFold–Making protein folding accessible to all. bioRxiv. 2021.08.15.456425

49. Simonetti B, Danson CM, Heesom KJ, Cullen PJ. Sequence-dependent cargo recognition by SNX-BARs mediates retromer-independent transport of CI-MPR. J Cell Biol. 2017; 216:3695–712. https://doi.org/10.1083/jcb.201703015 PMID: 28935633

50. Seaman MN, McCaffery JM, Emr SD. A membrane coat complex essential for endosome-to-Golgi retrograde transport in yeast. J Cell Biol. 1998; 142:665–81. https://doi.org/10.1083/jcb.142.3.665 PMID: 9700157

51. Simunovic M, Voth GA, Callan-Jones A, Bassereau P. When physics takes over: BAR proteins and membrane curvature. Trends Cell Biol. 2015; 25:780–92. https://doi.org/10.1016/j.tcb.2015.09.005 PMID: 26519988

52. Kvainickas A, Orgaz AJ, Nagele H, Diedrich B, Heesom KJ, Dengjel J, et al. Retromer- and WASH-dependent sorting of nutrient transporters requires a multivalent interaction network with ANKRD50. J Cell Sci. 2017; 130:382–95. https://doi.org/10.1242/jcs.196758 PMID: 27909246

53. Cozier GE, Carlton J, McGregor AH, Gleeson PA, Teasdale RD, Mellor H, et al. The phox homology (PX) domain-dependent, 3-phosphoinositide-mediated association of sorting nexin-1 with an early endosomal compartment of required for its ability to regulate EGF receptor degradation. J Biol Chem. 2002; 277:4873048736.

54. Chandra M, Chin YK, Mas C, Feathers JR, Paul B, Datta S, et al. Classification of the human phox homology (PX) domains based on their phosphoinositide binding specificities. Nat Commun. 2019; 10:1528. https://doi.org/10.1038/s41467-019-09355-y PMID: 30948714

55. Wassmer T, Attar N, Harterink M, van Weering JRT, Traer CJ, Oakley J, et al. The retromer coat complex coordinates endosomal sorting and dynein-mediated transport with carrier recognition by the trans-Golgi network. Dev Cell. 2009; 17:110–22. https://doi.org/10.1016/j.devcel.2009.04.016 PMID: 19619496

56. Hong Z, Yang Y, Zhang C, Niu Y, Li K, Zhao X, et al. The retromer component SNX6 interacts with dynactin p150(Glued) and mediates endosome-to-TGN transport. Cell Res. 2009; 19:1334–49. https://doi.org/10.1038/cr.2009.130 PMID: 19935774

57. Freeman CL, Hesketh G, Seaman MNJ. RME-8 coordinates the activity of the WASH complex with the function of the retromer SNX dimer to control endosomal tubulation. J Cell Sci. 2014; 127:2053–70. https://doi.org/10.1242/jcs.144659 PMID: 24643499

58. Schmid EM, McMahon HT. Integrating molecular and network biology to decode endocytosis. Nature. 2007; 448:883–8. https://doi.org/10.1038/nature06031 PMID: 17713526

59. Chandra M, Collins BM, Jackson LP. Biochemical basis for an interaction between SNX27 and the flexible SNX1 N-terminus. Adv Biol Regul. 2022; 83:100842. https://doi.org/10.1016/j.jbior.2021.100842

60. Yong X, Zhao L, Hu W, Sun Q, Ham H, Liu Z, et al. SNX27-FERM-SNX1 complex structure rationalizes divergent trafficking pathways by SNX17 and SNX27. Proc Natl Acad Sci U S A. 2021; 118(36): e2105510118. https://doi.org/10.1073/pnas.2105510118

61. Skruzny M, Pohl E, Gnoth S, Malengo G, Sourjik V. The protein architecture of the endocytic coat analysed by FRET microscopy. Mol Syst Biol. 2020; 16:e9009. https://doi.org/10.15252/msb.20199009 PMID: 32400111

62. Sun D, Varlakhanova N, Tornabene BA, et al. The cryo-EM structure of the SNX–BAR Mvp1 tetramer. Nat Commun. 2020; 11:1506. https://doi.org/10.1038/s41467-020-15110-5 PMID: 32198400

63. Cao TT, Deacon HW, Reczek D, Bretscher A, von Zastrow M. A kinase-regulated PDZ-domain interaction controls endocytic sorting of the beta2-adrenergic receptor. Nature. 1999; 410:286–90. https://doi.org/10.1038/45816 PMID: 10499588

64. Mao L, Liao C, Qin J, Gong Y, Zhou Y, Li S, et al. Phosphorylation of SNX27 by MAPK11/14 links cellular stress-signaling pathways with endocytic recycling. J Cell Biol. 2021; 220:e202010048. https://doi.org/10.1083/jcb.202010048 PMID: 33605979

65. Wang H, Qi W, Zou C, Xie Z, Zhang M, Naito MG, et al. NEK1-mediated retromer trafficking promotes blood-brain barrier integrity by regulating glucose metabolism and RIPK1 activation. Nat Commun. 2021; 12:4826. https://doi.org/10.1038/s41467-021-25157-7 PMID: 34376696

66. Itai N, Shimazu T, Kimura T, Ibe I, Yamashita R, Kaburagi Y, et al. The phosphorylation of sorting nexin 5 at serine 226 regulates retrograde transport and micropinocytosis. PLoS ONE. 2018; 13:e0207205. https://doi.org/10.1371/journal.pone.0207205 PMID: 30419003

67. Dephoure N, Zhou C, Villen J, Beausoleil SA, Bakalarski CE, Elledge SJ, et al. A quantitative atlas of mitotic phosphorylation. Proc Natl Acad Sci U S A. 2008; 105:10762–7. https://doi.org/10.1073/pnas.0805139105 PMID: 18669648

68. Zhou H, Di Palma S, Preisinger C, Peng M, Polat AN, Heck AJ, et al. Toward a comprehensive characterization of a human cancer cell phosphoproteome. Proteome Res. 2013; 12:260–71.

69. Bian Y, Song C, Cheng K, Dong M, Wang F, Huang J, et al. An enzyme assisted RP-RPLC approach for in-depth analysis of human liver phosphoproteome. Proteomics. 2014; 96:253–62. https://doi.org/10.1016/j.jprot.2013.11.014 PMID: 24275569

70. Koumandou VL, Klute MJ, Herman EK, Nunez-Miguel R, Dacks JB, Fields MC. Evolutionary reconstruction of the retromer complex and its function in Trypanosoma brucei. J Cell Sci. 2011; 124:1496–509. https://doi.org/10.1242/jcs.081596 PMID: 21502137

71. Suzuki SW, Chuang Y-S, Li M, Seaman MNJ, Emr SD. A bipartite sorting signal ensures specificity of retromer complex in membrane proteins recycling. J Cell Biol. 2019; 218:2876–86. https://doi.org/10.1083/jcb.201901019 PMID: 31337624

72. Norwood SJ, Shaw DJ, Cowieson NP, Owen DJ, Teasdale RD, Collins BM. Assembly and solution structure of the core retromer protein complex. Traffic. 2011; 12:56–71. https://doi.org/10.1111/j.1600-0854.2010.01124.x PMID: 20875039

73. Kvainickas A, Orgaz AJ, Nagele H, Hu Z, Dengjel J, Steinberg F. Cargo-selective SNX-BAR proteins mediate retromer trimer independent retrograde transport. J Cell Biol. 2017; 216:3677–93. https://doi.org/10.1083/jcb.201702137 PMID: 28935632

74. Rout MP, Field MC. The evolution of organellar coat complexes and organization of the eukaryotic cell. Annu Rev Biochem. 2017; 86:637–57. https://doi.org/10.1146/annurev-biochem-061516-044643 PMID: 28471691

75. Collins BM, Norwood SJ, Kerr MC, Mahony D, Seaman MN, Teasdale RD, et al. Structure of Vps26B and mapping of its interactions with the retromer protein complex. Traffic. 2008; 9:366–79. https://doi.org/10.1111/j.1600-0854.2007.00688.x PMID: 18088321

76. Eschenfeldt WH, Lucy S, Millard CS, Joachimiak A, Mark ID. A family of LIC vectors for high-throughput cloning and purification of proteins. Methods Mol Biol. 2009; 498:105–15. https://doi.org/10.1007/978-1-59745-196-3_7 PMID: 18988021

77. Mirdita M, Steinegger M, Soding J. MMseqs2 desktop and local web server app for fast, interactive sequence searches. Bioinformatics. 2019; 35:2856–8. https://doi.org/10.1093/bioinformatics/bty1057 PMID: 30615063

78. Hornak V, Abel R, Okur A, Strockbine B, Roitberg A, Simmerling C. Comparison of multiple Amber force fields and development of improved protein backbone parameters. Proteins. 2006; 65:712–25. https://doi.org/10.1002/prot.21123 PMID: 16981200

79. Ashkenazy H, Abadi S, Martz E, Chay O, Mayrose I, Pupko T, et al. ConSurf2016: an improved methodology to estimate and visualize evolutionary conservation in macromolecules. Nucleic Acids Res. 2016; 44:W344–50. https://doi.org/10.1093/nar/gkw408 PMID: 27166375

80. Ryan JF, Pang K, Schnitzler CE, Nguyen AD, Moreland RT, Simmons DK, et al. The genome of the ctenophore Mnemiopsis leidyi and its implications for cell type evolution. Science. 2013; 342:1242592. https://doi.org/10.1126/science.1242592 PMID: 24337300

81. Moreland RT, Nguyen AD, Ryan JF, Schnitzler CE, Koch BJ, Siewert K, et al. A customized Web portal for the genome of the ctenophore Mnemiopsis leidyi. BMC Genomics. 2014; 15:316. https://doi.org/10.1186/1471-2164-15-316 PMID: 24773765

82. Moreland RT, Nguyen AD, Ryan JF, Baxevanis AD. The Mnemiopsis Genome Project Portal: integrating new gene expression resources and improving data visualization. Database. 2020. https://doi.org/10.1093/database/baaa029 PMID: 32386298

83. Katoh K, Standley DM. MAFFT multiple sequence alignment software version 7: improvements in performance and usability. Mol Biol Evol. 2013; 30:772–80. https://doi.org/10.1093/molbev/mst010 PMID: 23329690

84. Minh BQ, Schmidt HA, Chernomor O, Schrempf D, Woodhams MD, Von Haeseler A, et al. IQ-TREE 2: new models and efficient methods for phylogenetic inference in the genomic era. Mol Biol Evol. 2020; 37:1530–4. https://doi.org/10.1093/molbev/msaa015 PMID: 32011700

85. Si Quang L, Gascuel O, Lartillot N. Empirical profile mixture models for phylogenetic reconstruction. Bioinformatics. 2008; 24:2317–23. https://doi.org/10.1093/bioinformatics/btn445 PMID: 18718941

86. Yang Z. Maximum likelihood phylogenetic estimation from DNA sequences with variable rates over sites: approximate methods. J Mol Evol. 1994; 39:306–14. https://doi.org/10.1007/BF00160154 PMID: 7932792

87. Yang Z. A space-time process model for the evolution of DNA sequences. Genetics. 1995; 139:993–1005. https://doi.org/10.1093/genetics/139.2.993 PMID: 7713447

88. Soubrier J, Steel M, Lee MS, Der Sarkissian C, Guindon S, Ho SY, et al. The influence of rate heterogeneity among sites on the time dependence of molecular rates. Mol Biol Evol. 2012; 29:3345–58. https://doi.org/10.1093/molbev/mss140 PMID: 22617951